

NGC 4388: A Test Case for Relativistic Disk Reflection and Fe K Fluorescence Features

Tahir Yaqoob^{1,2}, P. Tzanavaris^{1,2,3}, S. LaMassa⁴

¹Center for Space Science and Technology, University of Maryland, Baltimore County, 1000 Hilltop Circle, Baltimore, MD 21250, USA

²Center for Research and Exploration in Space Science and Technology, NASA/GSFC, Mail Code 662, Greenbelt, MD 20771, USA

³The American Physical Society, Hauppauge, New York 11788, USA

⁴Space Telescope Science Institute, 3700 San Martin Drive, Baltimore, MD 21218, USA

Received 2023

ABSTRACT

We present a new analysis of the *Suzaku* X-ray spectrum of the Compton-thin Seyfert 2 galaxy NGC 4388. The spectrum above ~ 2 keV can be described by a remarkably simple and rather mundane model, consisting of a uniform, neutral spherical distribution of matter, with a radial column density of $2.58 \pm 0.02 \times 10^{23} \text{ cm}^{-2}$, and an Fe abundance of $1.102^{+0.024}_{-0.021}$ relative to solar. The model does not require any phenomenological adjustments to self-consistently account for the low-energy extinction, the Fe $K\alpha$ and Fe $K\beta$ fluorescent emission lines, the Fe K edge, and the Compton-scattered continuum from the obscuring material. The spherical geometry is not a unique description, however, and the self-consistent, solar abundance MYTORUS model, applied with toroidal and non-toroidal geometries, gives equally good descriptions of the data. In all cases, the key features of the spectrum are so tightly locked together that for a wide range of parameters, a relativistic disk-reflection component contributes no more than $\sim 2\%$ to the net spectrum in the 2–20 keV band. We show that the commonly invoked explanations for weak X-ray reflection features, namely a truncated and/or very highly ionized disk, do not work for NGC 4388. If relativistically-broadened Fe $K\alpha$ lines and reflection are ubiquitous in Seyfert 1 galaxies, they should also be ubiquitous in Compton-thin Seyfert 2 galaxies. The case of NGC 4388 shows the need for similar studies of more Compton-thin AGN to ascertain whether this is true.

Key words: black hole physics - galaxies: active - radiation mechanisms: general - scattering - galaxies: individual:NGC 4388 - X-rays:galaxies

1 INTRODUCTION

It is nearly three decades since the first reports of relativistically-broadened Fe $K\alpha$ line emission in the X-ray spectra of active galactic nuclei (AGNs) with moderate spectral-resolution CCD detectors (Tanaka et al. 1995; Yaqoob et al. 1995). Since then, studies using the broad Fe $K\alpha$ lines, and associated reflection spectra, to probe the properties of the inner accretion disk and angular momentum (spin) of the central black-hole in AGN, have proliferated enormously, transforming the literature on AGN X-ray spectroscopy in a generation (e.g., see Reynolds 2019, 2021, and references therein). Originally, studies focussed on type 1, unobscured AGN because the X-ray spectra of obscured AGN are more complex, exhibiting line-of-sight extinction, as well as narrow Fe $K\alpha$ line emission and Compton-reflection continuum emission from nonrelativistic, distant matter. However, as modelling techniques for deconvolving the relativistic and nonrelativistic components improved, obscured AGN have been increasingly included alongside unobscured AGN for probing the inner accretion disk and black-hole spin (e.g., Tzanavaris et al. 2021, and references therein).

Over the years, relativistic disk-reflection models have become increasingly sophisticated, involving over a dozen parameters (e.g., see Dauser et al. 2013, 2022, and references therein), and it has now become common practice to *begin* modelling an AGN X-ray spectrum with the most complex scenarios, regardless of whether the data require such complexity or not. In particular, spectral-fitting with complex, over-parameterized models proceeds without testing whether a relativistically-broadened Fe $K\alpha$ line emission can actually be detected independently of the other features in the spectrum. There are so many parameters and freedom in the state-of-the-art disk-reflection models, that it is almost impossible that they will not fit the data. In the present paper we show results for an important case study of an AGN that should exhibit strong reflection and relativistically-broadened Fe fluorescence features according to standard models and expectations, but which in fact has an X-ray spectrum that has a very simple and mundane interpretation. The general principle that the case study highlights is that, in order to truly understand AGN X-ray spectra we must roll back the approach of immediately fitting the data with the most complex models available, and revert back to rigorously allowing the data to guide the model-fitting, as opposed to letting the models guide the analysis.

Many of the works on *Suzaku* observations of AGN were published before the existence of models that were able to self-consistently account for the Fe $K\alpha$ line emission and Compton-reflection from distant, nonrelativistic matter (e.g., see Nandra et al. 2007, and references therein). Such models enable disentanglement of the relativistic and distant-matter components. In the light of parallel improvements in the relativistic disk-reflection models since the *Suzaku* era, it is imperative to revisit some of the *Suzaku* observations to apply the newer methodologies. With this motivation, we have found that the *Suzaku* X-ray spectrum of the Seyfert 2 galaxy NGC 4388 is a very important test case. The original analysis of the *Suzaku* data presented by Shirai et al. (2008) fitted a host of heterogeneous, *ad hoc* models that included basic disk-reflection models that were available at the time, in combination with empirical model components. As with the analysis of many other AGN X-ray spectra at that time, there was no overall insight into a robust interpretation of the *Suzaku* X-ray spectrum of NGC 4388, given the approach of fitting *ad hoc* models that were unable to treat the physics self-consistently. The results of other historical studies of the same *Suzaku* spectrum of NGC 4388 are summarized in the appendix. We studied the same *Suzaku* spectral data of NGC 4388, and found that above ~ 2 keV, the spectrum can be very simply explained by extinction and reflection in a Compton-thin ($N_{\text{H}} < 1.25 \times 10^{24} \text{ cm}^{-2}$), uniform, neutral, solar-abundance, spherical distribution of matter, with no requirement for any relativistic disk emission component. Although the uniform spherical model is not a unique interpretation of the data, it is rare to be able to account for the Fe $K\alpha$ line and high-energy continuum in an AGN X-ray spectrum with such a simple model. This makes NGC 4388 an important reference source that generalized models of AGN involving disk-reflection spectra have to explain. For example, relativistic disk-reflection models fitted to AGN often require a factor of several overabundance in Fe (e.g., Garcıa et al. 2018, and references therein), yet our analysis of the *Suzaku* spectrum of NGC 4388 tightly constrains the Fe abundance to within 10% of solar. Our study enforces the condition that the Fe abundance in the disk and in distant matter cannot be different in the same astrophysical source. We are not aware of any similar study that enforces such a key condition. In the present paper we systematically derive upper limits to the contribution of a relativistic disk component contribution to the *Suzaku* spectrum of NGC 4388, for a wide range of parameter space, and find the contribution to be negligible.

The study in the present paper is restricted to the NGC 4388 *Suzaku* observation and focuses on the high-energy features in the spectrum above ~ 2 keV, although spectral-fitting analysis is performed down to ~ 0.6 keV. NGC 4388 is one of the brightest AGN in the X-ray band, so it has been observed by every X-ray astronomy mission since *ASCA*. The *Suzaku* spectrum still remains the best for simultaneously studying the Fe $K\alpha$ line, continuum absorption, and the Compton-reflected continuum. The latter requires coverage beyond 10 keV, out to at least 20 keV, and this condition is not satisfied by observations of NGC 4388 with *ASCA* (Iwasawa et al. 2007), *Chandra* (Shu et al. 2011; Yi et al. 2021, and references therein), *XMM-Newton* (Elvis et al. 2004; Beckmann et al. 2004), or *NICER* (Miller et al. 2019). Although *BeppoSAX* (Risaliti 2002) and *NuSTAR* (Masini et al. 2016; Kamraj et al. 2017; Ursini et al. 2019) do have the high-energy coverage, they have poor spectral resolution in the Fe $K\alpha$ emission-line and Fe-K region of the X-ray spectrum. In the present work, more detailed comparisons of our results from the *Suzaku* spectral analysis of NGC 4388 with results from previous studies of the same data and from observations with other X-ray astronomy missions can be found in the appendix. Here, we note only that the model-fitting of the spectra from other missions is very heterogeneous, and that none of the historical studies attempted to explain the high-energy X-ray spectra with a simple, uniform, spherical X-ray reprocessor.

The remainder of the present paper is organized as follows. In §2 we describe the data reduction procedures for constructing the spectra from the different *Suzaku* instruments, and for preparing the instrument spectral responses. In §3, we describe the spectral-fitting analysis, and present the results for spherical and other models of the distant matter distribution. In §4 we present the method and results for obtaining upper limits on the contribution of relativistic disk emission to the *Suzaku* X-ray spectrum of NGC 4388. Finally, in §5, we give a summary of results, and our conclusions. Relevant results from historical studies of NGC 4388 with different missions are summarized in the appendix.

2 DATA REDUCTION

The *Suzaku* data were reduced and analyzed in exactly the same way as described in Yaqoob et al. (2015) for Mkn 3 (including spectral extraction details and background subtraction methods). As for the case of Mkn 3, the GSO spectrum quality for NGC 4388 was too poor and unreliable to use for the detailed spectral study that is the goal of the present paper, so we rejected the GSO spectrum. The present study focuses on spectral data from the XIS CCD detector (Koyama et al. 2007) and the HXD PIN high-energy detector (Takahashi et al. 2007). Excluding lower and upper energy ranges that gave negative counts in the background-subtracted spectra, and the XIS range 2.1–2.45 keV due to known, large calibration systematics around the mirror Au M edges, resulted in the final energy ranges shown in Table 1, which also shows the background-subtracted count rates in these energy ranges. We note that the background-subtracted count rates for XIS and HXD/PIN are 85.9% and 35.8% respectively, of the net on-source count rates.

The absolute flux calibrations of the PIN and XIS have a systematic difference, and we denote the PIN:XIS cross-normalization ratio by $C_{\text{PIN:XIS}}$. The NGC 4388 observation was done in the so-called “XIS-nominal” pointing mode, and for this configuration, the recommended cross-normalization factor is 1.16 (see Yaqoob 2012, including a fuller discussion, covering situations that warrant deviations from this value). We fixed $C_{\text{PIN:XIS}}$ at the recommended value for all spectral-fitting analyses.

3 SPECTRAL FITTING ANALYSIS

One goal for the spectral-fitting analysis for NGC 4388 is to constrain both the line-of-sight and global column densities of matter surrounding the X-ray source, by modelling the Fe $K\alpha$ line emission self-consistently with respect to the X-ray absorption and Compton-scattered continuum

Table 1. Exposure Times and Count Rates for the *Suzaku* Spectra

Detector	Exposure (ks)	Energy Range (keV)	Rate ^a (ct/s)
XIS	112.4	0.6–2.1, 2.45–9.0	0.3984 ± 0.0011
PIN	104.4 ^b	14.0–40.8	0.217 ± 0.025

^a Background-subtracted count rate in the energy bands specified. ^b After dead-time correction.

(reflection) due to the same matter distribution. Such self-consistent modelling of the distant-matter features will reduce the degeneracy encountered with *ad hoc* models, when assessing the possible spectral contributions from features originating in matter that is closer to the putative black hole, such as relativistically broadened Fe $K\alpha$ line emission and reflection from an accretion disk (see §4). In §3.1 we describe the results of spectral fitting with a uniform spherical model of circumnuclear matter, and in §3.2 we give the results of fitting the MYTORUS model (Murphy & Yaqoob 2009). The latter model will also be used in a mode that is not restricted to a toroidal geometry. Since the MYTORUS spectral-fitting model was released, many other torus models have become available (Ikeda, Awaki, and Terashima 2009; Brightman and Nandra 2011; Liu and Li 2014; Furui et al. 2016; Baloković M. 2018; Buhner et al. 2019; Tanimoto et al. 2019). Descriptions and comparisons of different torus models can be found in Saha, Markowitz, and Buchner (2021), who conclude that, in general, current data are unable to distinguish between them.

We used XSPEC (Arnaud 1996) v12.11.1¹ for spectral fitting. Galactic absorption with a column density of $2.60 \times 10^{20} \text{ cm}^{-2}$ (Heiles and Cleary 1979) was included in all of the models. The same distant-matter models were used in the study of Mkn 3 (Yaqoob et al. 2015), and details of the various assumptions and caveats can be found there. In order to account for possible calibration systematics in the energy scale, and/or possible very mild ionization of the distant matter, we allowed the redshift parameter of the reprocessor models (z_R), to vary relative to the cosmological redshift of $z = 0.008419$ (Lu et al. 1993). The *Suzaku* CCD spectra can detect shifts in the Fe $K\alpha$ line peak that are as small as $\sim 10 \text{ eV}$. We note that a precision *Chandra* HETG measurement of the centroid energy of the Fe $K\alpha$ line in NGC 4388 of $6.393 \pm 0.004 \text{ keV}$ (Shu et al. 2011) constrains the line emitter to be essentially neutral.

The XSPEC convolution model GSMOOTH is used to apply velocity broadening to the intrinsic line widths. Details can be found in Yaqoob et al. (2015), including the relation between the model width parameter, σ_0 (keV), and the FWHM (km s^{-1}). In all of the models, the Fe $K\alpha$ line intensity and equivalent width (EW) are not free parameters because the line is produced self-consistently in the models. The models have no free parameters at all for the Fe $K\beta$ line because the line is calculated self-consistently with respect to the Fe $K\alpha$ line. Both the Fe $K\alpha$ and Fe $K\beta$ lines have an associated Compton shoulder, and each of these components have no free parameters because they are again calculated self-consistently with respect to the entire model.

The observed continuum fluxes, F_{obs} , and the observed (rest-frame) luminosities, L_{obs} , will be given in various energy bands. The intrinsic continuum luminosities, L_{intr} , were calculated by turning off all absorption and scattering components. For calculating luminosities, we use a standard, flat Λ CDM cosmology, adopting $H_0 = 73.3 \text{ km s}^{-1} \text{ Mpc}^{-1}$, and $\Omega_\Lambda = 0.70$ (Wong et al. 2020). All astrophysical model parameter values will be given in the rest frame of NGC 4388, unless otherwise stated.

3.1 Spectral Fits with a Uniform Spherical X-ray Reprocessor Model

In this section we model the circumnuclear matter in NGC 4388 with a very simple model consisting of a fully-covering uniform, neutral, spherical distribution of matter centered on the X-ray source, in which fluorescent line emission and the Compton-reflection continuum are calculated self-consistently. This is the simplest possible configuration of the global distribution of the X-ray reprocessor, and we use the model of Brightman and Nandra, 2011 (hereafter BN11). Historical observations of NGC 4388 going back over two decades show that energy of the prominent Fe $K\alpha$ emission line indicates that it originates in neutral matter (see appendix). The application of the BN11 model to NGC 4388 follows that for Mkn 3 (Yaqoob et al. 2015), and full details, its parameters, and various caveats, can be found in that study.

In addition to the BN11 model itself, the spectral data require other model components, none of which are unusual, as similar components are found in other AGN in general. One of these components is the second power-law continuum mentioned earlier, characterized by f_s , the fraction of the direct continuum that is scattered into the line of sight by optically-thin matter, extended on the same or larger size scale as the main X-ray reprocessor. Another spectral component included is thermal emission from optically-thin matter, and this is modelled using the XSPEC model APEC. In addition, we found it necessary to include spectral components for eight additional (narrow) emission or absorption features that were not accounted for by any of the other model components. For these, we used eight simple Gaussian components. Finally, a uniform, neutral, absorbing screen with column density $N_{H,1}$ (a free parameter), was applied to all of the spectral components. This column density may correspond to absorption in the host galaxy of NGC 4388 itself, and/or a small amount of additional absorption situated further out than the circumnuclear region modelled by the BN11 component. For the sake of reproducibility, we give the exact XSPEC model expression used to set up the model:

¹ <http://heasarc.gsfc.nasa.gov/docs/xanadu/xspec/>

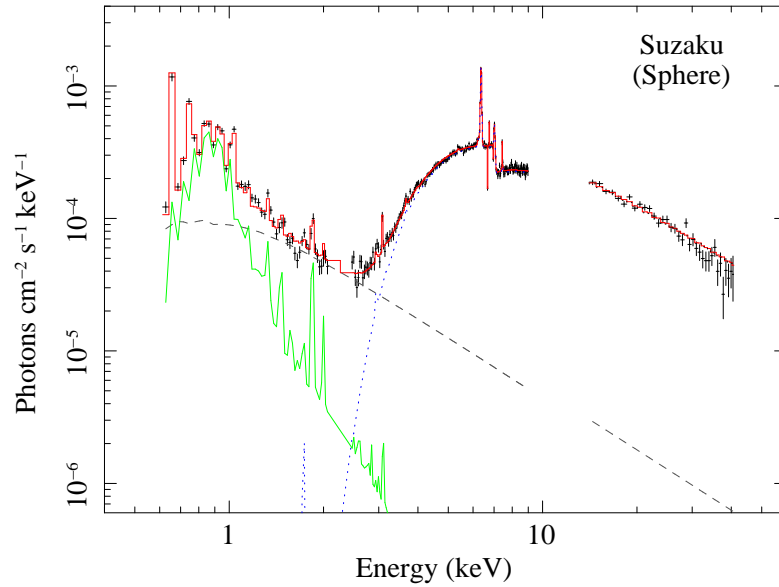


Figure 1. (a) Full, broadband spectral fit to the Suzaku NGC 4388 data with the best-fitting, uniform, neutral, spherical X-ray reprocessing model (see §3.1, Table 2). Shown are the unfolded spectrum (black), the net model spectrum (red) the contribution from the spherical X-ray reprocessor (dotted blue curve), the second power-law continuum (grey dashed line), and the optically-thin thermal emission (APEC) component (green). As noted in Yaqoob et al. (2015), “in an unfolded spectrum, some emission-line features appear to be artificially narrower than they really are”. The same fit overlaid instead on the counts spectrum in Fig. 2 does not suffer from this effect. Fig. 2 also shows the data/model ratios for this fit.

$$\begin{aligned}
 \text{model} = & \text{constant} \langle 1 \rangle * \text{phabs} \langle 2 \rangle * \text{zphabs} \langle 3 \rangle (+ \\
 & \text{gsmooth} \langle 4 \rangle * (\text{atable}\{\text{sphere0708.fits}\} \langle 5 \rangle) + \\
 & \text{constant} \langle 6 \rangle * \text{zpowerlw} \langle 7 \rangle + \text{apec} \langle 8 \rangle + \\
 & \sum_{n=9}^{n=17} \text{zgauss} \langle n \rangle) \quad (1)
 \end{aligned}$$

In the above expression, we identify $\text{constant} \langle 1 \rangle = C_{\text{PIN:XIS}}$, $\text{phabs} \langle 2 \rangle =$ Galactic column density, $\text{zphabs} \langle 3 \rangle = N_{\text{H},1}$, and $\text{constant} \langle 6 \rangle = f_s$ (associated with the distant scattering continuum). The $\text{apec} \langle 8 \rangle$ and $\text{zgauss} \langle n \rangle$ components refer to the optically-thin thermal continuum emission and the narrow Gaussian model features respectively. There are a total of 26 free parameters, but 16 of these are associated with the Gaussian components. The free parameters are the effective redshift of the BN11 model (z_{R}), the normalization of the intrinsic power-law continuum, its photon index (Γ), $N_{\text{H},1}$, N_{H} (radial column density), X_{Fe} (Fe abundance relative to solar), f_s , A_{apec} (normalization of the APEC component), kT_{apec} (temperature of the APEC component), the FWHM of the Fe $K\alpha$ line, the normalizations of the Gaussian emission/absorption components, and the center energies of the Gaussian emission/absorption components. The widths of the Gaussian components could not be constrained by the data and were fixed at 100 km s^{-1} FWHM, a value much less than the XIS spectral resolution.

The results are shown in Table 2, from which it can be seen that the reduced χ^2 value for the fit is 1.284, with a null probability of 4.55×10^{-4} . Fig. 1 shows the data and best-fitting unfolded photon spectrum. Fig. 2(a) shows the best-fitting model overlaid on the counts spectrum, and the corresponding data/model ratios are shown in Fig. 2(c). A zoomed view of the best-fitting model overlaid on the counts spectrum in the Fe K region is shown in Fig. 2(b), and the corresponding data/model ratios are shown in Fig. 2(d). It can be seen that the model provides an excellent fit to the data. In particular, the simple uniform spherical model of the absorption, fluorescent emission lines, and Compton-reflection continuum self-consistently accounts for the Fe $K\alpha$, Fe $K\beta$, the neutral Fe K edge, and continuum shape, and this is driven essentially by only two parameters, namely, N_{H} , and X_{Fe} . The only other components in the 5–8 keV band shown in Fig. 2(b) and Fig. 2(d) are weak narrow absorption lines due to Fe xxv(r), Fe xxvi, some additional Ni $K\alpha$ line emission, and a weak unidentified feature at $\sim 6.8 \text{ keV}$ (see Table 2). The best-fitting column density of the spherical model is $N_{\text{H}} = 25.78^{+0.19}_{-0.18} \times 10^{22} \text{ cm}^{-2}$, and $X_{\text{Fe}} = 1.102^{+0.024}_{-0.021}$. Both of these values are unremarkable, the column density indicating a source that is globally Compton-thin, and the Fe abundance is close to the Anders and Grevesse (1989) solar value. The difference is less than the systematic differences in solar Fe abundance that are reported in the literature (e.g. see Asplund et al. 2009). What is remarkable is that the model versus data plot in Fig. 2(b) and the fit residuals in Fig. 2(d) show that the data appear to leave no room for any broadened relativistic Fe $K\alpha$ line emission, and adding such a component to the model would only be fitting noise. Nevertheless, in §4 we present the results of adding reflection from a relativistic ionized disk to the model, in order to obtain upper limits on the flux of such a component.

The best-fitting value of $N_{\text{H},1}$ is $16.73^{+0.64}_{-0.65} \times 10^{20} \text{ cm}^{-2}$ (Table 2), which is more than two orders of magnitude less than the column

density of the spherical model component, N_{H} . The value of f_s obtained is $14.90^{+0.50}_{-0.45} \times 10^{-3}$. Both $N_{\text{H},1}$ and f_s are small enough that the self-consistency of the absorption, Compton scattering, and fluorescent line emission from the spherical model is not broken. It can be seen from Fig. 1 that the thermal optically-thin emission and the optically-thin scattered power-law continuum make a negligible contribution to the spectrum above ~ 3 keV, so these components of the model do not affect the fit parameters of the spherical reprocessor model. The temperature of the APEC component obtained from the fit is $kT_{\text{apec}} = 0.822^{+0.016}_{-0.017}$ keV. These values of kT_{apec} and f_s are consistent with historical results for extended emission in NGC 4388, as well as for similar AGN (see references in the appendix).

Table 2 shows that the Fe K α line flux and EW were measured to be 9.0×10^{-5} photons $\text{cm}^{-2} \text{s}^{-1}$, and 257 eV respectively, where the EW was calculated with respect to the total continuum at the line peak (in the AGN frame). Statistical errors on these two quantities were not calculated because the Fe K α line in the model is not separable, but the percentage errors will be similar to the corresponding errors for the MYTORUS fits described in §3.2. Those errors are of the order of 4%, on both the line flux and EW (see Table 2). The FWHM of the Fe K α line from the spherical model fit is 2855^{+725}_{-890} km s^{-1} , and this is entirely consistent with the *Chandra* HEG measurement of 2430^{+620}_{-590} km s^{-1} reported in Shu et al. (2011). We can estimate the characteristic radius of the line-emitting region using the simple prescription of Netzer (1990), and a black-hole mass for NGC 4388 of $1.58 \times 10^7 M_{\odot}$ (Woo and Urry 2002). This gives $r \sim 0.011$ pc and $r \sim 0.015$ pc for the *Suzaku* and *Chandra* HEG Fe K α line FWHM values respectively. This distance range corresponds to $\sim 1.5 - 2 \times 10^4$ gravitational radii.

Table 2 shows that the photon index of the intrinsic power-law continuum for the spherical model fit is $\Gamma = 1.513^{+0.006}_{-0.009}$, which is rather flat with respect to characteristic values of $\Gamma \sim 1.8-2.0$. However, statistical studies of AGN (both type 1 and type 2) do show a range in Γ of 1.5–2.5 (e.g., Dadina 2007, 2008; Baloković et al. 2020, and references therein). In addition, these studies show a non-negligible number of outliers outside of this range.

Continuum fluxes and luminosities obtained from the spherical model fit are shown in Table 3, in three energy bands: 0.5–2 keV, 2–10 keV, and 10–20 keV. These energy bands refer to the observed frame for fluxes, and to the source frame for luminosities. The 0.5–2 keV, 2–10 keV, and 10–20 keV fluxes are 0.475, 19.5, and 36.0×10^{-12} $\text{erg cm}^{-2} \text{s}^{-1}$ respectively. Observed and intrinsic luminosities are denoted by L_{obs} and L_{intr} respectively. The 0.5–2 keV, 2–10 keV, and 10–20 keV values for L_{obs} that we obtained are 0.067, 2.75, and 5.10×10^{42} erg s^{-1} respectively. The intrinsic luminosities in the 0.5–2 keV, 2–10 keV, and 10–20 keV bands are 3.16, 7.53, and 5.56×10^{42} erg s^{-1} respectively. Comparison of the intrinsic luminosities with corresponding values in the literature is complicated by the fact that they are often derived from *ad hoc* models, which can easily yield very different luminosities.

3.1.1 The Additional Gaussian Components

Table 2 shows the results for the eight Gaussian model components that were included in the spherical reprocessor model fit. Shown are the line centroid energies, fluxes, and equivalent widths (EW). There are six emission lines and two absorption lines (the latter have negative fluxes in Table 2). From comparison of the fitted energies with expected energies, we identify the emission-line components 1, 3, and 4 with O VIII Ly α , Ne VIII Ly α , and Ar XVIII Ly α respectively. Component 2 is unidentified, as is component 6. We have already mentioned the Gaussian components 5 to 8, which lie in the $\sim 6-8$ keV energy band, shown in Fig. 2(b). We identify components 5 and 7 with absorption due to Fe xxv(r) and Fe xxvi Ly α respectively. It is possible that all five components identified with highly ionized atomic species (components 1, 3, 4, 5, and 7) originate in the same ionized plasma, which may be nonuniform in ionization state and other physical properties. The emission lines would be produced by material out of the line-of-sight, and the two Fe absorption lines would be produced by material in the line-of-sight, possibly in the form of a wind. The statistical errors on the centroid energies are too large to allow a reliable determination of the outflow velocity of such a wind, but it could be as low as ~ 100 km s^{-1} , or as large as ~ 6300 km s^{-1} . Highly ionized species of Fe in outflow have been observed in other AGN (e.g., Tombesi 2015; Braitto et al. 2018, and references therein). We do not investigate the ionized outflow further with physical models, as it is beyond the scope of the present work. Future observations with the calorimeter aboard *XRISM* will provide higher spectral resolution data, which will be better for constraining the physics and geometry of the outflow.

We identify Gaussian component 8 with Ni K α fluorescence emission, which is likely produced in the same neutral matter that produces the Fe K α line. Even though the BN11 spherical model already includes Ni K α fluorescence emission, the non-zero flux of Gaussian component 8 implies that the BN11 model has a deficit in the Ni K α line flux. There is in fact considerable uncertainty in the solar value of the Ni abundance, so the need for additional Ni K α line flux in the model is not unexpected (e.g., see Yaqoob and Murphy 2011).

3.2 Spectral Fits with the MYTORUS Model

The ‘‘coupled’’ and ‘‘decoupled’’ modes of the MYTORUS spectral-fitting model for X-ray reprocessing (Murphy & Yaqoob 2009) have been described extensively in Yaqoob 2012, and LaMassa et al. 2014. The present application for NGC 4388 follows closely that for Mkn 3 (Yaqoob et al. 2015). Full details of the parameters, assumptions, and caveats can be found in that study, and we use the same particular MYTORUS model tables. The key parameters of the MYTORUS model are the normalization of the incident power-law continuum (A_{PL}), its photon index (Γ), the direct line-of-sight column density ($N_{\text{H,Z}}$), the global column density ($N_{\text{H,S}}$), and A_{S} , the relative normalization between the direct continuum and the reflected continuum (and fluorescent line emission). In coupled mode, by definition, both column densities are equal to the equatorial column density (e.g., Yaqoob et al. 2015), and the parameter θ_{obs} denotes the inclination angle of the line-of-sight to the observer with respect to the torus symmetry axes. In decoupled mode, the zeroth-order (i.e., direct) continuum is decoupled from the inclination angle (which becomes a dummy parameter), and the model can then crudely mimic different non-toroidal geometries. Velocity broadening of the

Table 2. Spectral-Fitting Results for Three X-ray Reprocessor Models

Parameter	Spherical (BN11)	MYTORUS (Coupled)	MYTORUS (Decoupled)
χ^2	409.50	398.32	396.47
Degrees of Freedom	319	318	318
Free Parameters	26	27	27
Reduced χ^2	1.284	1.253	1.247
Null probability	4.55×10^{-4}	1.46×10^{-3}	1.79×10^{-3}
$10^3 z_R$	$5.32^{+0.43}_{-0.42}$	$5.80^{+0.37}_{-0.50}$	$5.30^{+0.42}_{-0.41}$
Γ	$1.513^{+0.006}_{-0.009}$	$1.475^{+0.009}_{-0.006}$	$1.502^{+0.007}_{-0.008}$
$N_{H,1}$ (10^{20} cm $^{-2}$)	$16.73^{+0.64}_{-0.65}$	$25.6^{+1.6}_{-1.1}$	$29.85^{+1.65}_{-0.95}$
N_H [sphere] (10^{22} cm $^{-2}$)	$25.78^{+0.19}_{-0.18}$
$N_{H,S}$ (10^{22} cm $^{-2}$)	...	$32.05^{+0.25}_{-0.35}$	$60.0^{+3.7}_{-3.7}$
$N_{H,Z}$ (10^{22} cm $^{-2}$)	...	= $N_{H,S}$	$29.24^{+0.29}_{-0.24}$
A_S	...	$2.52^{+0.10}_{-0.08}$	$1.28^{+0.05}_{-0.04}$
Fe abundance (ratio to solar)	$1.102^{+0.024}_{-0.021}$	1.0(f)	1.0(f)
θ_{obs} ($^\circ$)	...	$77.20^{+0.40}_{-0.60}$...
$10^3 f_s$	$14.90^{+0.50}_{-0.45}$	$12.71^{+0.45}_{-0.40}$	$10.15^{+0.46}_{-0.31}$
kT_{apec} (keV)	$0.822^{+0.016}_{-0.017}$	$0.810^{+0.020}_{-0.018}$	$0.802^{+0.018}_{-0.018}$
A_{apec} (10^5 ph. cm $^{-2}$ s $^{-1}$ keV $^{-1}$)	$12.884^{+0.436}_{-0.434}$	$15.343^{+0.517}_{-0.613}$	$18.322^{+0.348}_{-0.732}$
Fe $K\alpha$ v_{shift} (km s $^{-1}$)	-916^{+128}_{-124}	-775^{+116}_{-148}	-923^{+125}_{-122}
Fe $K\alpha$ FWHM (km s $^{-1}$)	2855^{+725}_{-890}	3415^{+740}_{-590}	3415^{+460}_{-1295}
$I_{\text{Fe } K\alpha}$ (10^{-5} photons cm $^{-2}$ s $^{-1}$)	8.98	$8.66^{+0.34}_{-0.27}$	$8.66^{+0.34}_{-0.27}$
EW $_{\text{Fe } K\alpha}$ (eV)	257	255^{+10}_{-8}	255^{+10}_{-8}
E_1 (keV)	$0.668^{+0.004}_{-0.005}$	$0.669^{+0.005}_{-0.006}$	$0.668^{+0.006}_{-0.005}$
I_1 (10^{-5} photons cm $^{-2}$ s $^{-1}$)	$8.97^{+1.05}_{-1.04}$	$2.79^{+0.51}_{-0.39}$	$3.00^{+0.50}_{-0.50}$
EW $_1$ (eV)	504^{+59}_{-58}	157^{+29}_{-22}	182^{+30}_{-30}
E_2 (keV)	$0.749^{+0.005}_{-0.007}$	$0.748^{+0.008}_{-0.007}$	$0.748^{+0.008}_{-0.007}$
I_2 (10^{-5} photons cm $^{-2}$ s $^{-1}$)	$3.67^{+0.65}_{-0.65}$	$1.42^{+0.30}_{-0.31}$	$1.43^{+0.39}_{-0.24}$
EW $_2$ (eV)	238^{+42}_{-42}	92^{+19}_{-20}	100^{+28}_{-17}
E_3 (keV)	$1.056^{+0.009}_{-0.009}$	$1.054^{+0.009}_{-0.009}$	$1.054^{+0.009}_{-0.009}$
I_3 (10^{-5} photons cm $^{-2}$ s $^{-1}$)	$1.13^{+0.30}_{-0.19}$	$0.73^{+0.19}_{-0.15}$	$0.72^{+0.18}_{-0.15}$
EW $_3$ (eV)	113^{+30}_{-19}	73^{+15}_{-15}	78^{+15}_{-16}
E_4 (keV)	$3.117^{+0.050}_{-0.127}$	$3.003^{+0.057}_{-0.053}$	$3.002^{+0.052}_{-0.058}$
I_4 (10^{-5} photons cm $^{-2}$ s $^{-1}$)	$0.144^{+0.073}_{-0.076}$	$0.144^{+0.076}_{-0.074}$	$0.137^{+0.073}_{-0.077}$
EW $_4$ (eV)	$23.6^{+12.1}_{-12.5}$	$27.8^{+14.8}_{-14.8}$	$26.3^{+14.2}_{-14.8}$
E_5 (keV)	$6.721^{+0.031}_{-0.031}$	$6.722^{+0.038}_{-0.37}$	$6.722^{+0.027}_{-0.048}$
I_5 (10^{-5} photons cm $^{-2}$ s $^{-1}$)	$-0.544^{+0.174}_{-0.172}$	$-0.48^{+0.16}_{-0.19}$	$-0.51^{+0.17}_{-0.18}$
EW $_5$ (eV)	$-15.6^{+5.0}_{-4.9}$	$-13.6^{+4.5}_{-5.5}$	$-14.4^{+4.8}_{-5.2}$
E_6 (keV)	$6.822^{+0.032}_{-0.037}$	$6.832^{+0.029}_{-0.033}$	$6.832^{+0.033}_{-0.033}$
I_6 (10^{-5} photons cm $^{-2}$ s $^{-1}$)	$0.531^{+0.180}_{-0.187}$	$0.62^{+0.15}_{-0.22}$	$0.56^{+0.17}_{-0.20}$
EW $_6$ (eV)	$15.1^{+5.1}_{-5.3}$	$17.6^{+4.2}_{-6.3}$	$15.7^{+5.7}_{-4.7}$
E_7 (keV)	$7.020^{+0.073}_{-0.077}$	$6.991^{+0.070}_{-0.109}$	$6.970^{+0.078}_{-0.077}$
I_7 (10^{-5} photons cm $^{-2}$ s $^{-1}$)	$-0.289^{+0.187}_{-0.189}$	$-0.24^{+0.19}_{-0.19}$	$-0.26^{+0.17}_{-0.20}$
EW $_7$ (eV)	$7.0^{+4.0}_{-6.1}$	$-5.4^{+4.3}_{-4.2}$	$-6.5^{+3.0}_{-4.3}$
E_8 (keV)	$7.487^{+0.049}_{-0.041}$	$7.489^{+0.030}_{-0.029}$	$7.489^{+0.028}_{-0.026}$
I_8 (10^{-5} photons cm $^{-2}$ s $^{-1}$)	$0.372^{+0.178}_{-0.180}$	$0.65^{+0.20}_{-0.17}$	$0.70^{+0.16}_{-0.20}$
EW $_8$ (eV)	$16.4^{+7.9}_{-7.9}$	$28.9^{+8.7}_{-7.7}$	$31.2^{+9.4}_{-7.1}$

Spectral-fitting results for the *Suzaku* data for NGC 4388, with a uniform spherical model of the X-ray reprocessor (BN11), a toroidal model with MYTORUS, fitted in coupled mode, and a model with MYTORUS fitted in decoupled mode. See text for details. Fixed parameters are indicated by (f). The parameter z_R for X-ray reprocessing model components is fitted independently of the cosmological redshift, and it is used to derive the apparent velocity shift of the Fe $K\alpha$ line peak, v_{shift} . Parameter values for all other components are rest-frame values. The photon flux and EW of the Fe $K\alpha$ line are denoted by the parameters $I_{\text{Fe } K\alpha}$ and $\text{EW}_{\text{Fe } K\alpha}$ respectively. Note that for the BN11 model, the Fe $K\alpha$ line flux cannot be derived independently of the continuum, so the Fe $K\alpha$ line flux and EW are estimates only, and do not have statistical errors. The parameters I_n , and EW_n , where $n = 1$ to 8, denote the photon fluxes and EW values respectively, for the additional Gaussian emission or absorption lines that are included in all of the models. Parameters that have no entry in a particular column are not part of the model in that column.

Table 3. Fluxes and Luminosities from X-ray Reprocessor Spectral Fits

	Spherical (BN11)	MYTORUS (Coupled)	MYTORUS (Decoupled)
$F_{\text{obs}}[0.5\text{--}2 \text{ keV}]$ ($10^{-12} \text{ erg cm}^{-2} \text{ s}^{-1}$)	0.475	0.488	0.489
$F_{\text{obs}}[2\text{--}10 \text{ keV}]$ ($10^{-12} \text{ erg cm}^{-2} \text{ s}^{-1}$)	19.5	19.5	19.5
$F_{\text{obs}}[10\text{--}20 \text{ keV}]$ ($10^{-12} \text{ erg cm}^{-2} \text{ s}^{-1}$)	36.0	36.2	36.2
$L_{\text{obs}}[0.5\text{--}2 \text{ keV}]$ ($10^{40} \text{ erg s}^{-1}$)	6.73	7.44	7.50
$L_{\text{obs}}[2\text{--}10 \text{ keV}]$ ($10^{40} \text{ erg s}^{-1}$)	274.9	274.6	274.4
$L_{\text{obs}}[10\text{--}20 \text{ keV}]$ ($10^{40} \text{ erg s}^{-1}$)	510.4	513.4	513.6
$L_{\text{intr}}[0.5\text{--}2 \text{ keV}]$ ($10^{40} \text{ erg s}^{-1}$)	315.7	292.1	334.4
$L_{\text{intr}}[2\text{--}10 \text{ keV}]$ ($10^{40} \text{ erg s}^{-1}$)	752.9	736.9	806.0
$L_{\text{intr}}[10\text{--}20 \text{ keV}]$ ($10^{40} \text{ erg s}^{-1}$)	556.3	570.0	602.4

Fluxes and luminosities corresponding to the spectral-fitting results shown in Table 2, for the three X-ray reprocessor models, as described in the text. F_{obs} and L_{obs} are observed fluxes and luminosities, respectively. Intrinsic continuum luminosities, inferred by removing all absorption and scattering components, are denoted by L_{intr} .

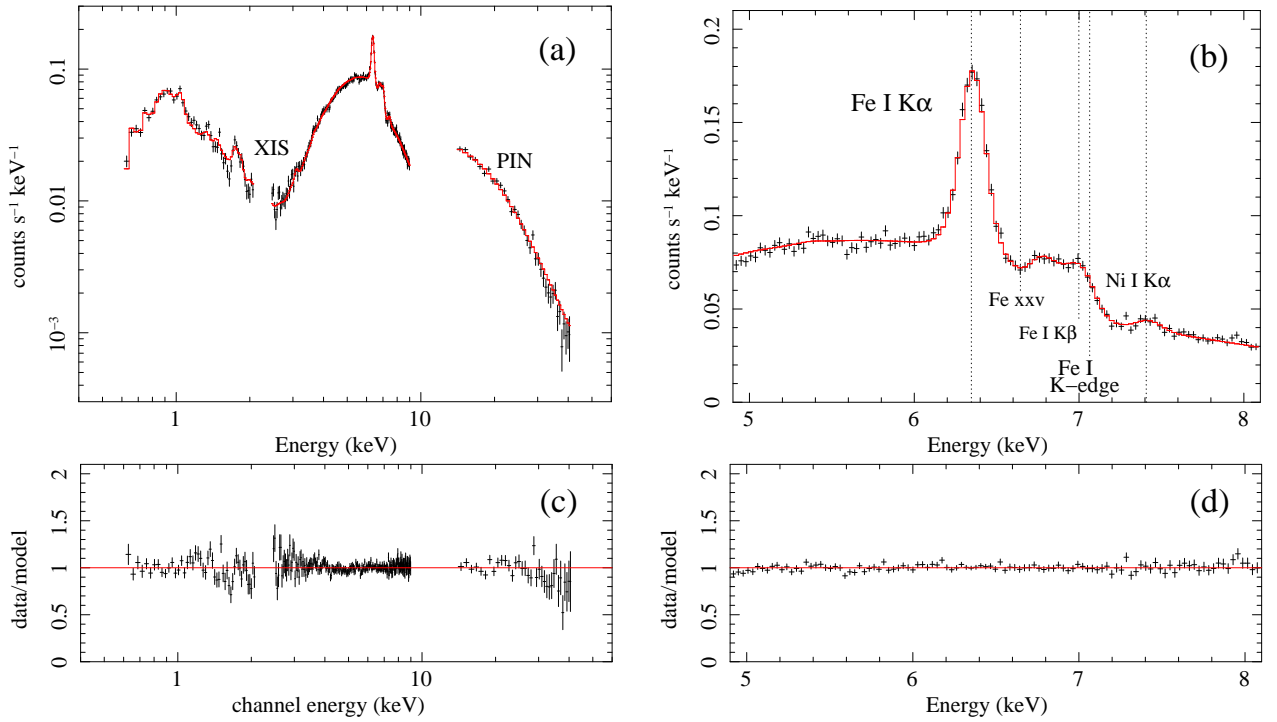


Figure 2. Same broadband spectral fit as in Fig. 1 (see §3.1 and Table 2), showing the uniform spherical X-ray reprocessor model fitted to the NGC 4388 *Suzaku* spectra. (a) The full broadband XIS and PIN data (black) overlaid with the best-fitting spherical (BN11) model (red). Caption text for panels (b), (c), and (d) as in Yaqoob et al. (2015): “(b) The data and model shown in (a), zoomed in on the Fe K region, showing the detailed fit to the Fe K α emission line and other atomic features, as labelled. Note that the flux of the model Fe K α line is not controlled by an arbitrary parameter, but calculated self-consistently from the same matter distribution that produces the global Compton-scattered continuum. The dotted lines correspond to the expected energies of the labelled atomic features in the observed frame. The data to model ratios corresponding to (a) and (b) are shown in (c) and (d) respectively”. Note that zoomed plots are shown specifically for the Fe K band, as opposed to the soft X-ray spectrum, because the purpose of the present paper is to constrain the matter distribution that produces the Fe K fluorescent lines, the line-of-sight extinction, and the Compton-scattered continuum. The spectral signatures from that material are insignificant below ~ 2 keV, (see Fig. 1), and the soft X-ray spectrum originates in different material. Consequently, the constraints on the high-energy spectrum are not sensitive to the details of how the soft X-ray spectrum is modelled.

MYTORUS emission components is implemented in the same way as it was for the BN11 spherical model, and we also include the same additional spectral components corresponding to optically-thin scattering, optically-thin thermal emission, and the eight empirical Gaussian components (see §3.1). We present the results of fitting the *Suzaku* NGC 4388 spectra with the coupled and decoupled MYTORUS models in §3.2.1 and §3.2.2 respectively.

3.2.1 Coupled MYTORUS Model

The XSPEC model expression for the coupled MYTORUS model that was applied to the NGC 4388 spectra is:

Table 4. Relativistic Disk Model Fractional Contribution Upper Limits

$\cos \theta_{\text{obs}}$	R_X^a	$\log \xi$	f_{UR} (a=0.0) broadband	f_{UR} (a=0.9982) broadband	f_{UR} (a=0.0) (> 3 keV)	f_{UR} (a=0.9982) (> 3 keV)
0.95	0.5	0.0	0.95026	1.01198	1.13870	1.36835
0.95	0.5	1.0	0.95486	1.02123	1.14640	1.38676
0.95	0.5	2.0	0.98103	1.05204	1.18192	1.45730
0.95	0.5	3.0	0.90902	0.93055	1.02292	1.19616
0.95	0.5	4.0	0.79524	0.79525	0.70773	0.68441
0.95	1.0	0.0	0.96188	1.07286	1.50038	2.09108
0.95	1.0	1.0	0.96955	1.08824	1.49876	2.07085
0.95	1.0	2.0	1.00952	1.13436	1.39816	1.90382
0.95	1.0	3.0	0.91801	0.96112	0.99252	1.13419
0.95	1.0	4.0	0.78598	0.78756	0.75590	0.74346
0.95	2.0	0.0	0.93796	1.10267	1.19436	1.61013
0.95	2.0	1.0	0.95179	1.12518	1.20829	1.64392
0.95	2.0	2.0	0.99630	1.19572	1.26090	1.76053
0.95	2.0	3.0	0.91929	0.98395	1.00714	1.20027
0.95	2.0	4.0	0.78602	0.77517	0.70306	0.68443
0.95	3.0	0.0	0.91601	1.10831	1.51258	2.06379
0.95	3.0	1.0	0.92520	1.12518	1.50479	2.04676
0.95	3.0	2.0	0.97882	1.19572	1.40267	1.89232
0.95	3.0	3.0	0.91143	0.98996	1.01585	1.16683
0.95	3.0	4.0	0.78603	0.77675	0.75435	0.73879
0.05	0.5	0.0	1.08170	1.10789	1.29876	1.36906
0.05	0.5	1.0	1.08322	1.10632	1.31105	1.38280
0.05	0.5	2.0	1.04314	1.06319	1.36644	1.46093
0.05	0.5	3.0	0.92045	0.95921	1.11891	1.22387
0.05	0.5	4.0	0.82301	0.81990	0.69373	0.68910
0.05	1.0	0.0	1.15345	1.23235	1.84501	2.10342
0.05	1.0	1.0	1.15494	1.22924	1.88070	2.09555
0.05	1.0	2.0	1.10113	1.16186	1.71892	1.93663
0.05	1.0	3.0	0.94212	1.03043	1.06880	1.15754
0.05	1.0	4.0	0.82148	0.82616	0.75125	0.75128
0.05	2.0	0.0	1.18648	1.23235	1.42997	1.65975
0.05	2.0	1.0	1.18797	1.22924	1.45310	1.69654
0.05	2.0	2.0	1.12354	1.16186	1.54558	1.82209
0.05	2.0	3.0	0.96379	1.03043	1.10767	1.23877
0.05	2.0	4.0	0.82461	0.82616	0.68750	0.96706
0.05	3.0	0.0	1.18604	1.23182	1.89572	2.07447
0.05	3.0	1.0	1.18598	1.22564	1.88018	2.05900
0.05	3.0	2.0	1.12010	1.16295	1.72010	1.92037
0.05	3.0	3.0	0.97152	1.04745	1.09835	1.21041
0.05	3.0	4.0	0.82306	0.82772	0.74657	0.75128

The upper limits on the percentage contribution of relativistic disk reflection to the *Suzaku* spectra of NGC 4388, when the disk reflection is modelled with RELXILL, and included with a uniform spherical model for the distant-matter Compton reflection and Fe K line emission (see text for details). Shown are values of f_{UR} , defined as the upper limit on the percentage of the 2–20 keV total observed flux that is due to only the RELXILL component, for a given set of RELXILL model parameters. The values of f_{UR} are shown for 80 combinations of the key RELXILL parameters, a (dimensionless black-hole spin), cosine of the inclination angle ($\cos \theta_{\text{obs}}$), reflection fraction (R_X), and the logarithm of the ionization parameter ($\log \xi$). The corresponding values of the remaining RELXILL model parameters are given in the text. Columns 4 and 5 show values of f_{UR} obtained from the broadband spectral fits, whereas columns 6 and 7 show the values of f_{UR} obtained from the fits performed on data above 3 keV. In the latter case, the values of f_{UR} were calculated by extrapolating each model down to 2 keV.

$$\begin{aligned}
\text{MYTORUS model} = & \text{a constant} < 1 > * \text{phabs} < 2 > (\\
& \text{zpowerlw} < 3 > * \text{etable}\{\text{mytorus_Ezero_v00.fits}\} < 4 > + \\
& \text{constant} < 5 > * (\text{gsmoothb} < 6 > (\text{atable}\{\text{mytorus_scatteredH200_v00.fits}\} < 7 >)) + \\
& \text{constant} < 8 > * (\text{gsmooth} < 9 > (\text{atable}\{\text{mytl_V000010nEp000H200_v00.fits}\} < 10 >)) + \\
& \text{constant} < 11 > * \text{zpowerlw} < 12 > + \text{zphabs} < 13 > * \text{apec} < 14 > +
\end{aligned}$$

$$\sum_{n=15}^{n=23} \text{zgauss} < n > \quad (2)$$

(3)

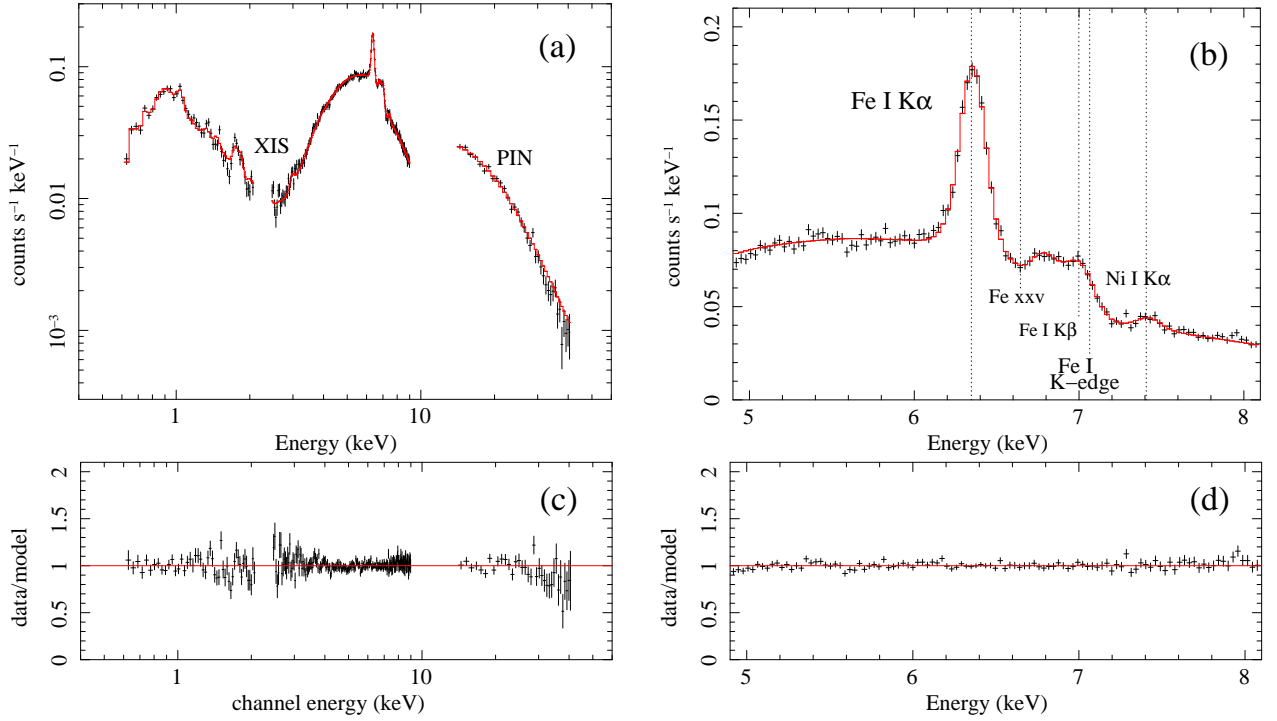


Figure 3. Broadband spectral fit to the NGC 4388 *Suzaku* spectra with the coupled MYTORUS model (see §3.2.1 and Table 2). All of the descriptions in the caption for Fig. 2 apply here.

Here we identify constant $\langle 1 \rangle = C_{\text{PIN:XIS}}$, phabs $\langle 2 \rangle =$ Galactic column density, constant $\langle 5 \rangle = A_S =$ constant $\langle 8 \rangle$, and constant $\langle 11 \rangle = f_s$. In coupled mode, the column densities associated with each of the three MYTORUS model tables (components 4, 7, and 10 above) are tied together, as are the inclination angles. The corresponding parameters of the two Gaussian velocity broadening components, gsmooth $\langle 6 \rangle$ and gsmooth $\langle 9 \rangle$, are tied together. Note that, whereas the BN11 spectral fit included an additional (thin) absorbing screen that covered all emission components, we found that it was only required for the optically-thin thermal emission component in the MYTORUS fit. The column density of this component is again denoted by $N_{\text{H},1}$ (component 13 on the model expression). There are a total 27 free parameters in the fit, one more than in the BN11 fit (again, 16 of these parameters are associated with the Gaussian components). The spectral-fitting results are given in Table 2, from which it can be seen that the χ^2 value for the fit is 398.32 (corresponding to a reduced χ^2 value of 1.253), with a null probability of 1.46×10^{-3} . Fig. 3(a) shows the best-fitting model overlaid on the counts spectrum, and the corresponding data/model ratios are shown in Fig. 3(c). A zoomed view of the best-fitting model overlaid on the counts spectrum in the Fe K region is shown in Fig. 3(b), and the corresponding data/model ratios are shown in Fig. 3(d). It can be seen that the model provides an excellent fit to the data, with no significant residuals in the Fe K band. Although the MYTORUS fit is formally statistically marginally better than the spherical model fit, we do not interpret the results as favoring one geometry over the other. This is because the complex soft X-ray spectral modelling for both cases needs improvement, in terms of better data and models, and the most important aspect for the present study is that both models leave no statistically significant residuals in the critical Fe K band. The inclination angle and column density from the coupled MYTORUS fit are $(77.20^{+0.40}_{-0.60})^\circ$ and $3.205^{+0.025}_{-0.035} \times 10^{23} \text{ cm}^{-2}$ respectively. As noted in Murphy and Yaqoob (2009), this column density should be multiplied by $\pi/4$ in order to compare with the radial column density from the BN11 spherical model. Taking this into account, the coupled torus model column density is in good agreement with the column density obtained from the uniform spherical model. The value of the constant $A_S = 2.52^{+0.10}_{-0.08}$ is more than double the value for a time-steady intrinsic X-ray continuum illuminating a torus with a covering factor of 0.5. The value of f_s for the coupled MYTORUS fit is $12.71^{+0.45}_{-0.40} \times 10^{-3}$, or $\sim 15\%$ lower than the corresponding value for the BN11 fit. The intrinsic power-law continuum is a little flatter than it is in the BN11 fit, with $\Gamma = 1.475^{+0.009}_{-0.006}$.

The magnitude of the shift of the peak of Fe $K\alpha$ emission line is $\sim 15\%$ lower than it is for the BN11 model, with non-overlapping statistical errors. However, the flux and EW of the line are similar for the two models, and statistically consistent with each other. The FWHM of the Fe $K\alpha$ line is formally $\sim 20\%$ higher from the coupled MYTORUS fit, but it is still statistically consistent with both the BN11 fit to the *Suzaku* spectra and the historical *Chandra* HETG measurement described in §3.1. In addition, the centroid energies, fluxes, and EW values of all eight Gaussian line components are all statistically consistent with the corresponding values from the BN11 fit, and the same is true of the temperature of the optically-thin thermal continuum (kT_{apecc}). However, the relative normalization of the latter emission component from the MYTORUS fit is $\sim 19\%$ higher than it is for the BN11 fit. On the other hand, all of the net observed fluxes and luminosities agree within 11% for the BN11 and coupled MYTORUS models. The intrinsic luminosities are not expected to be similar, since they are model-dependent.

Nevertheless, our fits show that they are similar within $\sim 8\%$ for the two models. The column density, $N_{\text{H},1}$, associated with the APEC component is $25.6_{-1.1}^{+1.6} \times 10^{20} \text{ cm}^{-2}$, the same order of magnitude as the uniform screen applied in the BN11 model.

3.2.2 Decoupled MYTORUS Model

In decoupled mode, the XSPEC model expression is the same as that for the coupled mode (§3.2.1), except that the column density for the zeroth-order continuum, $N_{\text{H},Z}$ (associated with component 4), is independent of the global column density, $N_{\text{H},S}$ (associated with components 7 and 10), which is responsible for producing the Compton-scattered continuum and the fluorescent line emission respectively. As explained in Yaqoob (2012), and Yaqoob et al. (2015), in decoupled mode, the inclination angle associated with the zeroth-order continuum is a dummy parameter, fixed at 90° , and for the reflected spectrum the data are not sensitive to the associated inclination angle if all of the column densities involved are Compton-thin. The spectral fits to NGC 4388 so far show that all of the column densities are indeed Compton-thin, so we simply choose to fix the inclination angle associated with the reflection spectrum and fluorescent line emission tables at 0° .

The spectral-fitting results for the decoupled model fit are given in the fourth column of Table 2, from which it can be seen that the χ^2 value for the fit is 396.47 (corresponding to a reduced χ^2 value of 1.247), with a null probability of 1.79×10^{-3} . The difference in χ^2 between the coupled and decoupled MYTORUS models is < 2 , for the same number of free parameters, so the decoupled MYTORUS fit is essentially statistically indistinguishable from the coupled fit. Fig. 3(a) shows the best-fitting decoupled model overlaid on the counts spectrum, and the corresponding data/model ratios are shown in Fig. 3(c). A zoomed view of the best-fitting model overlaid on the counts spectrum in the Fe K region is shown in Fig. 3(b), and the corresponding data/model ratios are shown in Fig. 3(d). It can be seen that the model again provides an excellent fit to the data, with no significant residuals in the Fe K band. The global column density is $N_{\text{H},S} = 60.0_{-3.7}^{+3.7} \times 10^{22} \text{ cm}^{-2}$, which is a factor of ~ 2 larger than the equatorial column density from the coupled MYTORUS fit. The parameter A_S is $1.28_{-0.04}^{+0.05}$, a factor of ~ 2 smaller than that from the coupled MYTORUS fit. The column density in the line-of-sight is $N_{\text{H},Z} = 29.24_{-0.24}^{+0.29} \times 10^{22} \text{ cm}^{-2}$, which is similar to the equatorial column density from the coupled MYTORUS fit, and similar to the radial column density from the spherical model fit.

The intrinsic continuum photon index is $1.502_{-0.008}^{+0.007}$, similar to that obtained from the other two fits, and $f_s = 10.15_{-0.31}^{+0.46} \times 10^{-3}$, which is $\sim 20\%$ lower than the corresponding value from the coupled MYTORUS fit. The temperature of the optically-thin emission, kT_{apex} , is statistically consistent with that obtained from both of the other fits, but its normalization is $\sim 19\%$ higher than that from the coupled MYTORUS fit. The shift of the peak of the Fe $K\alpha$ line is statistically consistent with that obtained from the BN11 fit, but is $\sim 19\%$ higher than that from the coupled MYTORUS fit. On the other hand, the FWHM of the Fe $K\alpha$ line, its flux, and EW, are all statistically indistinguishable between the coupled and decoupled MYTORUS fits. Likewise, the centroid energies, fluxes, and EW values of all eight Gaussian components are also statistically indistinguishable between the coupled and decoupled MYTORUS fits. The observed continuum fluxes and luminosities are all consistent within 1% between the coupled and decoupled MYTORUS fits, but the intrinsic luminosities appear to be systematically higher for the decoupled MYTORUS fits, by $\sim 6\%$ to 11% .

In Fig. 5, the best-fitting components of the MYTORUS coupled and decoupled models are directly compared with each other. The red dotted curves show the zeroth-order continua, and the blue dot-dashed curves show the Compton-scattered continua. The grey dashed lines show the optically-thin scattered power-law continua. The solid black curves show the sums of these separate components, including the Fe $K\alpha$ line emission. The separate contributions from the Fe $K\alpha$ line and the eight Gaussian components, as well as the optically-thin thermal emission, are not shown for the sake of clarity, since the purpose of the plot is to compare the MYTORUS continuum components. It can be seen that the observed X-ray spectrum of NGC 4388 above ~ 4 keV is dominated by the line-of-sight column density, as opposed to the Compton-scattered continuum from the global matter distribution. However, the latter is the continuum linked to the observed Fe $K\alpha$ emission line because it involves the same global matter distribution as the line emitter. The solid angle subtended by the line-of-sight material is negligible, so it cannot produce any significant Fe $K\alpha$ line emission. Fig. 5 also shows that the zeroth-order spectral components for the coupled and decoupled MYTORUS fits are very similar, as are the Compton-scattered continuum components.

4 CONSTRAINTS ON A RELATIVISTIC DISK CONTRIBUTION TO THE X-RAY SPECTRUM

We have shown that the *Suzaku* nuclear X-ray spectrum of NGC 4388 above ~ 2 keV can be explained with a model that is as simple as a uniform, spherically-symmetric, solar-abundance matter distribution that is more than 10^4 gravitational radii from the putative central black hole. The data/model residuals in the Fe K band after fitting any of the nonrelativistic models described thus far, are such that adding a relativistic disk model to such fits would simply be fitting noise (see Figs. 2, 3, and 4). This implies that there is no requirement for a relativistically-broadened Fe $K\alpha$ emission line. Nevertheless, we can quantify upper limits on the relative contribution of a reflection spectrum from a relativistic accretion disk. For the latter we use the ionized, relativistic disk-reflection model RELXILL, which is described in detail in García et al. (2014), and commonly applied to the X-ray spectra of accreting sources. We add this model to the uniform, spherical (BN11) model of distant matter described in §3.1. Since the best-fitting BN11 model has a marginally higher fit statistic than the two MYTORUS model fits, using the BN11 model as the baseline for the relativistic disk fit will provide a more stringent test for the presence of any disk component in the X-ray spectrum. In addition, the BN11 model allows us to tie the Fe abundance in the distant matter, to that in the disk. Generally, we are addressing the question of why there appear to be no signatures of the accretion disk in the X-ray spectrum of NGC 4388, and therefore, we are searching for scenarios in which the upper limit on the disk contribution allowed by the data is as large as possible.

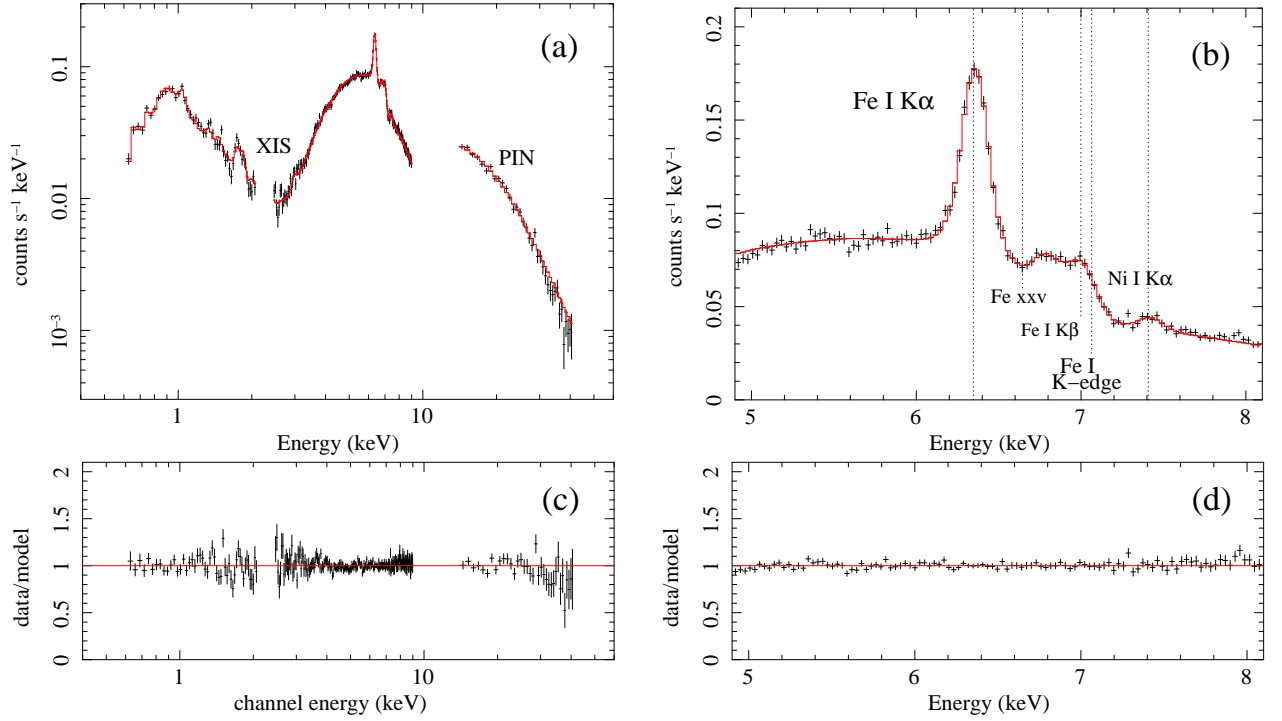


Figure 4. Broadband spectral fit to the NGC 4388 *Suzaku* spectra with the decoupled MYTORUS model (see §3.2.2 and Table 2). All of the descriptions in the caption for Fig. 2 apply here.

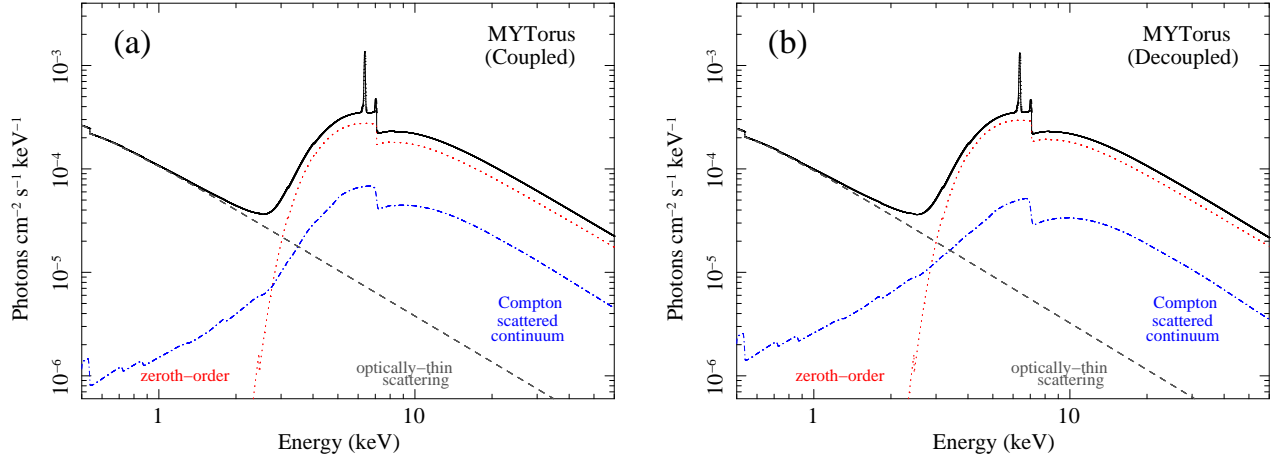


Figure 5. A comparison of the principal model components for (a) the coupled MYTORUS model, and (b) the decoupled MYTORUS model (see Table 2). In each panel, the grey dashed line is the second power-law continuum, due to optically-thin scattering, the red dotted curve shows the zeroth-order continuum, the blue dot-dashed curve shows the MYTORUS Compton-scattered continuum, and the solid black curve is the net spectrum. The latter includes the Fe $K\alpha$ and Fe $K\beta$ emission lines. However, the individual emission-line components and the APEC thermal continuum are omitted for clarity (see text for details).

The RELXILL model has 14 parameters, although one of these is the cosmological redshift, which is fixed at the value given in §1. Since the BN11 model fit leaves no margin for any significant spectral complexity (especially in the Fe K band), the RELXILL parameters cannot be constrained if too many of them are free. Therefore, we take the approach of selecting a wide range of combinations of the RELXILL parameters, freezing all except the overall normalization of the RELXILL component, and studying the upper limits on that normalization as a function of the unique sets of combinations of the other parameters. Specifically, for each unique parameter set, we vary the RELXILL overall normalization until the χ^2 value relative to the BN11 baseline fit increases by 2.706, corresponding to 90% confidence for one free parameter. We now briefly describe each of the other 12 parameters, and their treatment for the study.

Disk radial emissivity parameters: q_1 , q_2 , r_{BR} . The radial emissivity in the RELXILL model is described by a broken power law, with power-law indices q_1 and q_2 for radii $\leq r_{BR}$ and $> r_{BR}$ respectively (r_{BR} is simply the “break radius” at which the power-law index switches between q_1 and q_2). Observationally, the radial emissivity is poorly constrained in AGN in general, and from a theoretical point-of-view, there is a wide range of possibilities. It is challenging to constrain the slope of even a single power-law emissivity parameterization for most AGN,

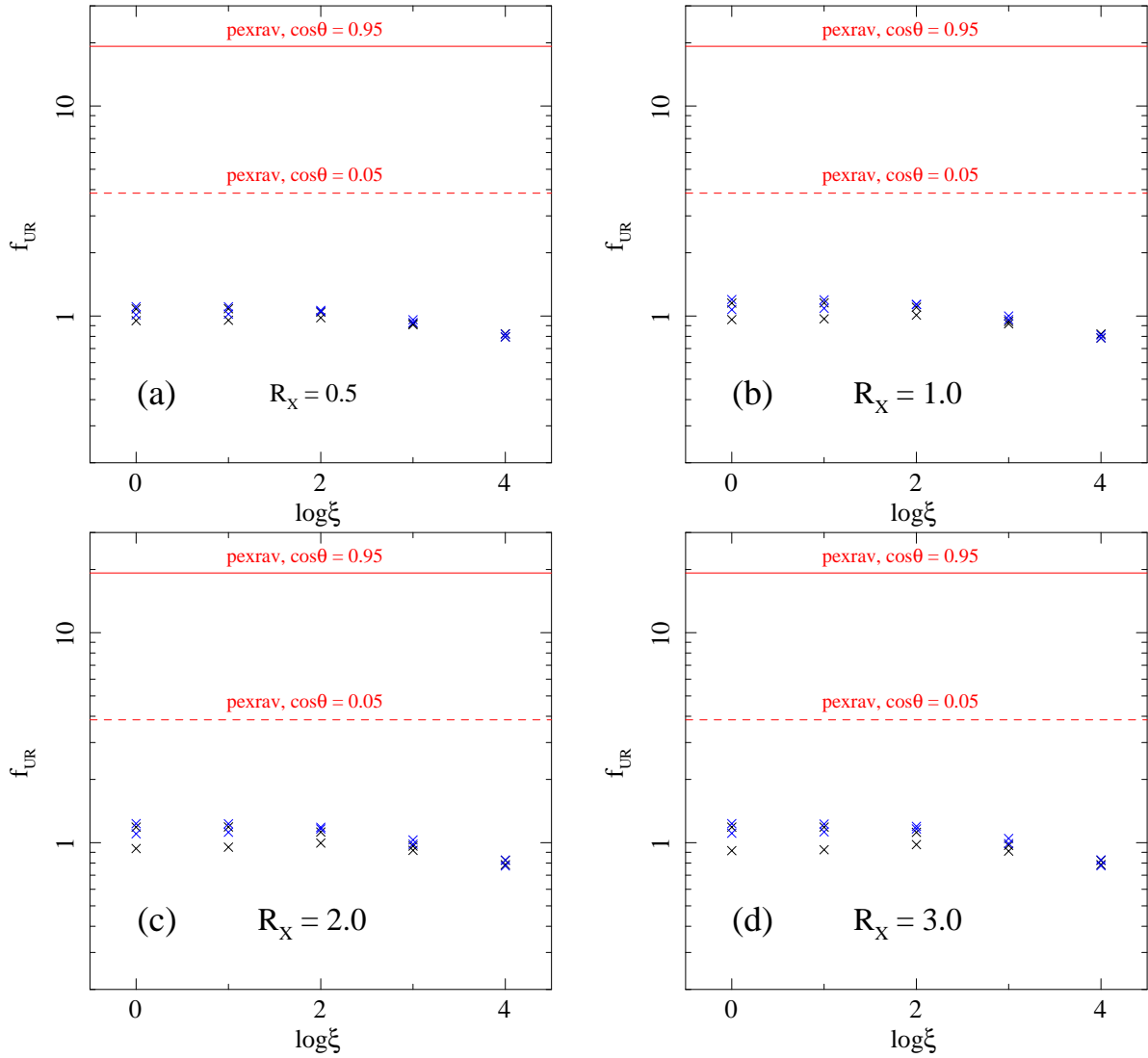


Figure 6. The upper limits on the 2–20 keV flux contribution of the disk-reflection component, f_{UR} , as a percentage of the total 2–20 keV flux (the latter includes the reflection and the uniform spherical model), versus the logarithm of the disk ionization parameter, $\log \xi$. The values of f_{UR} and $\log \xi$ are from Table 4, and were obtained from fitting the NGC 4388 *Suzaku* spectra with the uniform spherical model and the ionized disk-reflection model, RELXILL, as described in the text. Panels (a), (b), (c), and (d) show the results for the four values of the RELXILL parameter, R_X , of 0.5, 1.0, 2.0, and 3.0, respectively. Black and blue crosses correspond to black-hole spin values of $a = 0$ and $a = 0.9982$ respectively. For clarity, the two inclination angles corresponding to $\cos \theta_{\text{obs}} = 0.05$ and $\cos \theta_{\text{obs}} = 0.95$ (see Table 4), are not distinguished in the plots because there would be even greater overlap of the different symbols, due to the weak dependence of f_{UR} on the inclination angle. As familiar benchmarks, in comparison, each panel also shows horizontal lines corresponding to the equivalent 2–20 keV flux percentage contributions for the PEXRAV model, for the extremal inclination angles, θ , corresponding to $\cos \theta = 0.05$ (red, dashed lines), and $\cos \theta = 0.95$ (red, solid lines).

and this is true of NGC 4388 as well, so it has to be fixed. In our fits we use a single power-law function for the radial emissivity by tying q_1 and q_2 together and fixing the index at a value of 3.0 (the value of r_{BR} is then irrelevant, but we fix it at $15r_g$). The value of 3.0 for q_1 ($= q_2$) is that expected for the outer parts of a Shakura and Sunyaev disk (e.g., Laor 1991; Dauser et al. 2013). Studies of samples of AGN find that emissivity indices do not often go below 2.0, and emissivity indices greater than 3.0 are required by some AGN (e.g., Walton et al. 2013). A steeper radial emissivity law would produce a stronger reflection spectrum from the inner disk, and therefore, *smaller* upper limits on the RELXILL component contribution to the net X-ray spectrum. The present study aims to establish the largest possible contributions of the disk-reflection spectrum, so an emissivity index of 3.0 is appropriate.

Intrinsic continuum photon index: Γ . The intrinsic continuum in the RELXILL model is a power law with an exponential high-energy cut-off. The photon index, Γ , is tied to the corresponding photon index of the BN11 model.

Cut-off energy: E_{cut} . This is fixed at 300 keV. It is beyond the bandpass of the data and does not affect the fit. Nevertheless, it is consistent with the findings from studies of samples of AGN observed by *BeppoSAX* (Dadina 2007, 2008), and *NuSTAR* (Baloković et al. 2020).

Iron abundance relative to solar: X_{Fe} . This is tied to the relative iron abundance in the BN11 model.

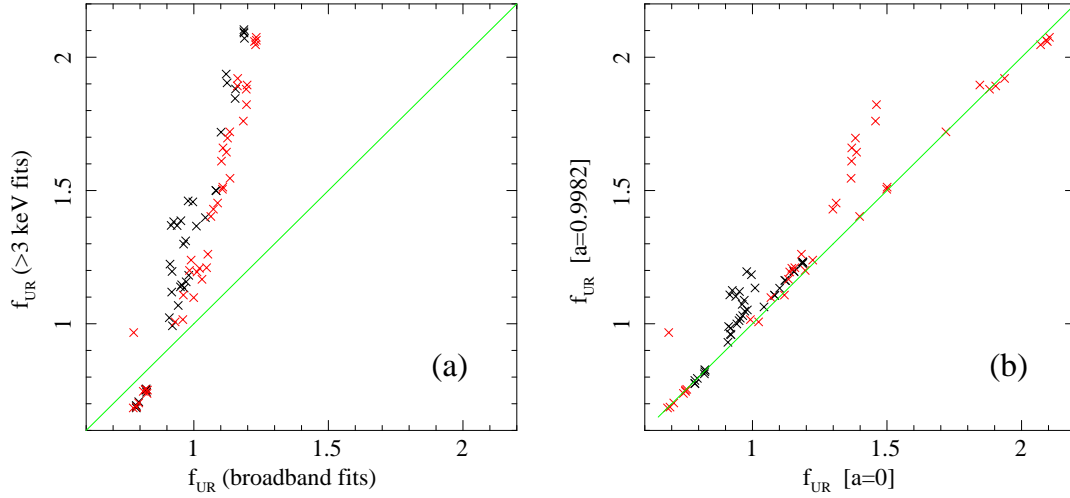


Figure 7. (a) From Table 4, the values of the percentage contributions of the disk-reflection model component, f_{UR} , obtained from the high-energy fits above 3 keV, versus the corresponding values obtained from the broadband fits. (b) The effect of the black-hole spin parameter, a , on the values of f_{UR} . Shown are the percentage contributions of the disk-reflection model component, f_{UR} , in Table 4, for the black-hole spin parameter, a , equal to the extremal upper value of 0.9982, versus the values of f_{UR} obtained for a equal to the extremal lower value of 0. In each panel, the green line is the locus of points that have equal values of f_{UR} .

Black-hole spin: a . The two extremal values for this dimensionless black-hole spin parameter are selected, namely 0.0, and 0.9982, the latter corresponding to the maximal value for an accreting black hole (Thorne 1974).

Inner disk radius: R_{in} . This parameter is set to -1, which means that the RELXILL model will use a value for the inner disk radius that corresponds to the inner-most stable orbit for the value of black-hole spin selected. This is aligned with our goal of obtaining the largest upper limits on a disk-reflection contribution to the X-ray spectrum of NGC 4388, because we are investigating what contribution the data allow, given that the reflection appears to be absent. Setting R_{in} to larger values (and thereby emulating a disk with a truncated inner edge), would make the Fe $K\alpha$ emission-line narrower, which would in turn *reduce* the upper limit on a disk-reflection contribution. This is because the Fe $K\alpha$ line in the NGC 4388 data is already fully accounted for by the distant-matter contribution, and it is locked in by the other spectral signatures of the distant matter.

Outer disk radius: R_{out} . The outer disk radius is fixed at $1000r_g$, the maximum value in the the model table. Relativistic features in the spectrum are formed within tens of gravitational radii, and if the outer radius were confined to such small values, smaller upper limits would be obtained on the RELXILL normalization. Therefore, the choice of $1000r_g$ will give the largest upper limits on the latter.

Disk inclination angle: θ_{obs} . Valid inclination angles of the disk in the RELXILL model lie in the range $0.95 \geq \cos \theta_{\text{obs}} \geq 0.05$, and we select the two extremal values, corresponding to 18.2° and 87.1° respectively.

Logarithm of the ionization parameter: $\log \xi$. The ionization parameter is essentially the ratio of incident ionizing flux on the disk to the ion number density. We select five values of $\log \xi$: 0.0, 1.0, 2.0, 3.0, and 4.0. The lowest value corresponds to an essentially neutral disk, and the highest value corresponds to a completely ionized disk.

Reflection fraction: R_X . This is not the same as the relative reflection strength in standard nonrelativistic disk models such as PEXRAV (Magdziarz and Zdziarski, 1995). Dauser et al. (2016) explain in great detail the meaning of R_X in the RELXILL model, and how it compares with other models and definitions of the relative magnitude of the reflection spectrum compared to the intrinsic continuum (see also Dauser et al. 2014). For RELXILL, R_X is essentially the ratio of the coronal intensity that illuminates the disk to the coronal intensity that reaches the observer. Unlike other definitions of the reflection fraction, R_X does not depend on the inclination angle, nor the physical condition of the disk. We select four values for R_X , namely, 0.5, 1.0, 2.0, and 3.0. Considering that the NGC 4388 data do not require any reflection, this range more than covers the scenarios of interest (see Dauser et al. 2016).

Thus, there are 80 unique combinations of parameters: two values of black-hole spin, two values of disk inclination angle, four values of R_X , and five values of $\log \xi$. This will lead to 80 corresponding upper limits on the contribution of the RELXILL component to the overall X-ray spectrum of NGC 4388. This number of parameter combinations avoids an overwhelming number of spectral fits, yet spans a wide enough parameter space to cover a plausible range of scenarios. In each of the 80 spectral fits, all of the BN11 parameters that were free in the analysis with only the BN11 model (§3.1) remain free, and in the RELXILL component, only the RELXILL overall normalization is free. Each of the fits begins with a best-fitting value of the RELXILL normalization of 0.0, and the upper limit of that normalization is obtained as described above.

The RELXILL normalization parameter by itself is not very informative. Instead, we introduce a quantity derived from it, f_{UR} , defined as the upper limit on the percentage of the 2–20 keV net flux that is in the RELXILL component, where the net flux includes the BN11 and RELXILL components. Thus, f_{UR} is a measure of the maximum percentage contribution of the relativistic disk component to the total 2–20 keV spectrum that is allowed by the data (at the 90% confidence level), for a given set of the other RELXILL parameters, aside from

its normalization. In order to place values of f_{UR} in a familiar context, we can calculate an analogous 2–20 keV flux contribution for the commonly used nonrelativistic disk-reflection model, PEXRAV, which can be directly compared with f_{UR} obtained from the NGC 4388 fits with RELXILL. We calculate that flux percentage for PEXRAV for the extremal values of the disk inclination angle, 18.2° and 87.1° , both for a PEXRAV reflection fraction, R , of 1.0. For this calculation, we set the photon index of the intrinsic power-law continuum, Γ , to the best-fitting value found from the BN11 spherical model fit (Table 2). We will refer to these two benchmark PEXRAV flux percentages as f_{PB1} and f_{PB2} for disk inclination angles 18.2° and 87.1° , respectively. The values of f_{PB1} and f_{PB2} are calculated to be 3.845% and 19.238% respectively. Thus, near face-on and edge-on nonrelativistic, neutral, reflection contributes less than $\sim 4\%$ and $\sim 20\%$ to the net 2–20 keV flux, respectively. Note that the PEXRAV model does not include any fluorescent line emission.

The 80 values of f_{UR} that we obtained from the 80 configurations of the BN11 and RELXILL models applied to NGC 4388 are shown in Table 4. The same 80 values of f_{UR} are shown in Fig. 6, plotted against $\log \xi$, separated into four panels by the value of R_X , as indicated in each panel. For direct comparison, each panel of Fig. 6 also shows the two PEXRAV benchmarks, f_{PB1} and f_{PB2} . It can be seen from Table 4 and Fig. 6, that the values of f_{UR} are clustered within the range $\sim 1 \pm 0.25\%$ across the entire parameter space that is probed. The values of f_{UR} appear to be insensitive to R_X , but are systematically lower for the largest value of the ionization parameter. It can also be seen that all values of f_{UR} are a factor of ~ 3 smaller than the lowest PEXRAV benchmark, and nearly a factor 20 smaller than the highest PEXRAV benchmark.

It could be argued that it is the soft part of the X-ray spectrum that is constraining the disk-reflection spectrum to be negligible, as opposed to the lack of a relativistically broadened Fe $K\alpha$ emission-line component. In order to address this, we repeated the entire analysis described above, using only the spectral data above 3 keV. Since f_{UR} is defined by fluxes in the 2–20 keV band, models fitted above 3 keV were extrapolated down to 2 keV in order to calculate f_{UR} . This approximation has a negligible effect on f_{UR} , compared to the differences in the f_{UR} values between the broadband and higher energy fits. The numerical results for f_{UR} are shown in columns 6 and 7 in Table 4, and Fig. 7(a) shows the values f_{UR} obtained from the fits above 3 keV, plotted against the corresponding values from the broadband fits. It can be seen that the values of f_{UR} obtained from the fits above 3 keV are indeed systematically higher than those obtained from the broadband fits, where f_{UR} for the latter is $< 1.9\%$. However, even in the worst case, for the fits above 3 keV, $f_{\text{UR}} < 2.1\%$, which is still nearly an order of magnitude less than the face-on PEXRAV benchmark value (see Fig. 6).

Fig. 7(a) also shows that there is a relatively narrow range in f_{UR} , regardless of the values of any of the RELXILL parameters that were varied. The black and red data points in Fig. 7(a) correspond to fits with the black-hole spin equal to 0.0 and the maximum, 0.9982, respectively, and it can be seen that the fits above 3 keV tend to have slightly higher values of f_{UR} for $a=0.0$ than for $a = 0.9982$. Fig. 7(b) shows the dependence on black-hole spin in a different way, in which values of f_{UR} for the maximum spin are plotted against corresponding values for the minimum spin. Values of f_{UR} from the broadband fits are shown in black, whereas those from the fits above 3 keV are shown in red. It can be seen that for most cases, the black-hole spin does not affect f_{UR} , but there are clusters of data points for which the maximum spin gives values of f_{UR} that are higher than the corresponding values for $a = 0$. However, the difference is never more than 30%.

5 CONCLUSIONS

We have presented the results of a new analysis of the *Suzaku* X-ray spectrum of the Compton-thin Seyfert 2 galaxy NGC 4388. We have applied new models and methodologies that did not exist at the time that results from this observation were first published, and have not been applied in several subsequent analyses of the same data (see appendix). Our study focusses on features above ~ 2 keV, in order to investigate whether a relativistically-broadened Fe $K\alpha$ line and associated Compton-reflection continuum, originating in an accretion disk, are present in the X-ray spectrum. With modern techniques, these broad features that are commonly reported in type 1 AGN, should just as easily be detectable in Compton-thin type 2 AGN. In order to achieve this, features from distant matter (thousands of gravitational radii or more from the central black hole), namely the narrow Fe $K\alpha$ line and its associated Compton-reflection continuum, should be modelled self-consistently, along with any line-of-sight absorption.

We applied three models for the neutral distant-matter components of the spectrum: a uniform, spherical distribution of matter (using the BN11 model of Brightman and Nandra, 2011), and two variations of the MYTORUS reprocessor model (Murphy and Yaqoob, 2009). We found that the uniform spherical model provided an excellent fit to the data, yielding an Fe abundance that is $1.102^{+0.024}_{-0.021}$ relative to solar. The best-fitting radial column density for this model is $2.58 \pm 0.02 \times 10^{23} \text{ cm}^{-2}$. The simple model simultaneously accounts for the flux and equivalent width of the Fe $K\alpha$ line, the associated Compton-reflection continuum, the detailed spectral shape in the Fe-K edge region, and line-of-sight absorption. These features fit well without any *ad hoc* adjustments to the model, aside from additional Ni $K\alpha$ line emission (likely due to a Ni overabundance), and an absorption line at ~ 6.7 keV due to He-like Fe resonance absorption in an ionized wind, possibly associated with the accretion disk. The uniform spherical model is not a unique description of the data. We also fitted two variations of the MYTORUS model, both having a fixed solar Fe abundance, and found that these models could not be ruled out. Again, the models simultaneously account for the key features in the high-energy spectrum, without phenomenological adjustments.

The residuals between the data and all three of the distant-matter models are essentially noise, so that there is no need for any relativistic disk-reflection component. We proceeded to quantify this by taking the spherical model fit as a baseline, and systematically finding upper limits on the contribution of a disk-reflection component, in the form of the RELXILL model, for a wide range in parameter space. We found that the upper limits on the contribution of such a component are not significant, and are remarkably insensitive to the model parameters. Formally, in the 2–20 keV band, the disk-reflection component never contributes more than $\sim 10\%$ and $\sim 25\%$ of standard PEXRAV reflection continua

with a reflection fraction of 1.0, for the most face-on and edge-on orientations respectively. Given that a uniform spherical distribution is a viable configuration of the X-ray obscuring matter in NGC 4388, we cannot conclude that the orientation of the accretion disk relative to the observer is edge-on or nearly edge-on. Indeed, there is no evidence for supporting any particular orientation of the accretion disk in NGC 4388.

Despite the fact that most historical X-ray spectral studies of NGC 4388 are based on phenomenological models that lack self-consistency, our tight upper limits on the relativistic disk-reflection component are in broad agreement with those obtained from the simpler historical modelling. All except the very first *Suzaku* study (Shirai et al. 2008) found that a reflection continuum was either relatively weak or negligible (see appendix for details, and references therein). However, since we have shown that the line-of-sight absorption, the Fe $K\alpha$ and Fe $K\beta$ emission lines, Compton-scattered continuum, and detailed Fe K edge structure from that obscuring material are all tightly locked together, there are two very important implications. One is that a disk with a truncated inner edge cannot explain the weak disk-reflection component. This is because truncation makes the Fe $K\alpha$ narrower, but the strength of the Fe $K\alpha$ line is already locked in by the other properties of the material that produces the line. Therefore, a truncated disk would give even smaller upper limits on the contribution of a disk-reflection component to the net spectrum. The second implication is that a very high disk ionization cannot explain the lack of relativistically-broadened Fe $K\alpha$ line. Our analysis included completely ionized states of the disk, yet the upper limits on the disk contribution to the net spectrum were still small. This is because the shape of the disk spectrum across the energy bandpass is sufficiently different to that required by the data, and the self-consistent spectral components from the obscuring material cannot be perturbed significantly by the incongruent disk spectrum. Both a truncated disk and a highly ionized disk are commonly invoked whenever a disk-reflection component is absent when one was expected (Reynolds et al. 2021, and references therein).

A simple spherical X-ray reprocessor has never been fitted to the X-ray spectrum of NGC 4388 from any mission. In general, our analysis highlights the need to carefully consider which models may be most appropriate to apply to a particular source, and whether complex models are uniquely required to describe the data better than simpler ones. If relativistically-broadened Fe $K\alpha$ line emission and reflection are ubiquitous features in type 1 AGN, they should also be ubiquitous in Compton-thin AGN, because the tools for deconvolving the nonrelativistic features have improved since the early days of CCD X-ray spectroscopy. Traditionally, it has been thought that type 1 AGN are better for studying relativistically-broadened Fe $K\alpha$ lines and the X-ray reflection continuum. However, somewhat counterintuitively, Compton-thin AGN can be better in some cases, because the line-of-sight extinction, signatures from the global matter distribution, and the strong narrow Fe $K\alpha$ emission line are strongly locked together. When these are fitted with self-consistent models, it results in better constraints on any broad-line component, whereas type 1 AGN have a narrow Fe $K\alpha$ that cannot be anchored by associated absorption and scattering features. Moreover, in Compton-thin AGN, the very complex soft X-ray portion (below $\sim 2\text{--}4$ keV) of the disk-reflection spectrum is suppressed, because it is absorbed by more distant matter, considerably facilitating the spectral deconvolution problem for disentangling the disk and distant-matter features.

More Compton-thin AGN should be re-examined along the lines that we have presented for NGC 4388 (see also Tzanavaris et al. 2021), to test whether they systematically have a dearth of relativistic signatures in the X-ray spectra. Two of the most common explanations do not work for NGC 4388. In addition to the specific reasons given for NGC 4388 above, in general, it would be problematic if Compton-thin AGN were universally required to have truncated and/or extremely ionized disks, because current unification models of type 1 and type 2 AGN insist that there is no difference in the central engine for the classification of AGN type. We have also noted that the Fe abundance in distant matter cannot be wildly different to the Fe abundance in the accretion disk in the same AGN. This is another advantage of using Compton-thin AGN to study or search for relativistic disk signatures, because the Fe abundance can be strongly constrained by the multiple features from distant matter, and it can be tied to the disk Fe abundance for spectral fitting. However, as far as we are aware, this fact has never been utilized for studies reported in the current literature. Moreover, a very high Fe over-abundance is often required as an unavoidable price to pay for accounting for an observed broad Fe $K\alpha$ line in an AGN or X-ray binary system. There is no evidence for supersolar abundances in other parts of these systems or the host galaxy, yet an Fe overabundance as high as a factor of ~ 8 in the accretion disk is not considered unusual in these studies (e.g., see Reynolds 2021, and references therein). In one case, overabundances of 10 to 20 (for different models), were invoked for a particular AGN (see García et al. 2018, and references therein). However, none of these studies has ever applied self-consistent models of the distant-matter spectrum to constrain the Fe abundance in the disk. In fact, the Fe abundance in the distant matter and in the accretion disk *cannot* be tied together if the distant-matter model components are empirical and/or *ad hoc*. The case of NGC 4388 should prompt theoretical studies that examine the current paradigms more critically.

The considerations discussed above will be all the more important for forthcoming *XRISM* data for AGN in general, because *XRISM* has no hard X-ray detector with high throughput coverage above 12 keV, so a critical portion of the Compton-reflection continuum will be missing. Only a limited number of observations are likely to have simultaneous coverage with *NuSTAR*. On the other hand, the superior *XRISM* spectral resolution in the Fe K band will improve the ability to deconvolve the distant-matter features. The Fe abundance will play a critical role in these studies, and the greater sensitivity of the *XRISM* calorimeter to narrow Ni $K\alpha$ line emission will elevate the importance of the role of the Ni abundance as well (e.g., see Yaqoob and Murphy 2011; Fukazawa et al. 2016).

ACKNOWLEDGEMENTS

The authors thank T. J. Turner, A. Scholtes, M. Trevor, and M. M. Tatum for their contribution to this work. This work was supported by NASA grants NNX10AE83G and 80GSFC21M0002. P.T. also acknowledges support from NASA grant 80NSSC18K0408 (solicitation NNH17ZDA001N-ADAP). This research has made use of data and software provided by the High Energy Astrophysics Science Archive

Research Center (HEASARC), which is a service of the Astrophysics Science Division at NASA/GSFC and the High Energy Astrophysics Division of the Smithsonian Astrophysical Observatory.

DATA AVAILABILITY

The data underlying this article will be shared on reasonable request to the corresponding author.

This paper has been typeset from a $\text{\TeX}/\text{\LaTeX}$ file prepared by the author.

REFERENCES

- Anders E., Grevesse N., 1989, *Geochimica et Cosmochimica Acta*, 53, 197
- Arnaud K. A., 1996, in Jacoby G, Barnes J, eds., *ASP Conf. Ser. Vol. 101, Astronomical Data Analysis Software and Systems V*. Astron. Soc. Pac., San Francisco, p. 17
- Asplund M., Grevesse N., Sauval A. J., and Scott P., 2009, *ARA&A*, 47, 481
- Baloković M. et al., 2018, *ApJ*, 854, 42
- Baloković M. et al., 2020, *ApJ*, 905, 41
- Beckmann V., Gehrels N., Favre P., Walter R., Courvoisier T. J.-L., Petrucci P.-O., Malzac J., 2004, *ApJ*, 614, 641
- Braito V. et al., 2018, *MNRAS*, 479, 3592
- Brightman M., Nandra K., 2011, *MNRAS*, 413, 1206 (BN11)
- Dadina M., 2007, *A&A*, 461, 1209
- Dadina M., 2008, *A&A*, 485, 417
- Dauser T., García J. A., Joyce A., Lickleder S., Connors R. M. T., Ingram A., Reynolds C. S., Wilms J., 2022, *MNRAS*, 514, 3965
- Dauser T., García J., Parker M. L., Fabian A. C., Wilms J., 2014, *MNRAS*, 444, L100
- Dauser T., García J., Walton D. J., Eikmann W., Kallman T., McClintock J., Wilms J., 2016, *A&A*, 590, A76
- Dauser T., García J., Wilms J., Böck M., Brenneman L. W., Falanga M., Fukumura K., Reynolds C. S., 2013, *MNRAS*, 430, 169
- Elvis M., Risaliti G., Nicastro F., Miller J. M., Fiore F., Puccetti S., 2004, *ApJ*, 615, L25
- Fabian A. C., Rees M. J., Stella L., White N. E., 1989, *MNRAS*, 238, 729
- Fedorova E. V., Beckmann V., Neronov A., Soldi S., 2011, *MNRAS*, 417, 1140
- Fukazawa Y. et al., 2011, *ApJ*, 727, 19
- Fukazawa Y., Furui S., Hayashi K., Ohno M., Higari K., Noda H., 2016, *ApJ*, 821, 15
- Furui S., Fukazawa Y., Odaka H., Kawaguchi T., Ohno M., Hayashi K., 2016, *ApJ*, 818, 164
- García J. et al., 2014, *ApJ*, 782, 76
- García J., Kallman T. R., Bautista M., Mendoza C., Deprince J., Palmeri P., Quintet P., 2018, in Mendoza C., Turck-Chièze S., Colgan J., eds., *ASP Conf. Ser. Vol. 515, Astrophysical Opacities*. Astron. Soc. Pac., San Francisco, p. 282
- Heiles C., Cleary M. N., 1979, *Australian J. Phys. Astrophys. Suppl.*, 47, 1
- Ikeda S., Awaki H., Terashima Y., 2009, *ApJ*, 692, 608
- Iwasawa K., Fabian A. C., Ueno S., Awaki H., Fukazawa Y., Matsushita K., Makishima K., 1997, *MNRAS*, 285, 683
- Kamraj N., Rivers E., Harrison F. A., Brightman M., Baloković M., 2017, *ApJ*, 843, 89
- Kawamuro T., Ueda Y., Tazaki F., Ricci C., Terashima Y., 2016, *ApJ*, 225, 14
- Laor A., 1991, *ApJ*, 376, 90
- Liu Y., Li X., 2014, *ApJ*, 787, 52
- Lu N. Y., Hoffman G. L., Groff T., Roos T., Lamphier T., 1993, *ApJS*, 88, 383
- Lubiński P. et al., 2016, *MNRAS*, 458, 2454
- Magdziarz P., Zdziarski A. A., 1995, *MNRAS*, 273, 837
- Masini A. et al., 2016, *A&A*, 589, 59
- Miller J. M., Kammoun E., Ludlam R. M., Gendreau K., Arzoumanian Z., Cackett E., Tombesi F., 2019, *ApJ*, 884, 106
- Miyazawa T., Haba Y., Kunieda H., 2009, *PASJ*, 61, 1331
- Murphy K. D., Yaqoob T., 2009, *MNRAS*, 397, 1549
- Nandra K., O’Neill P. M., George I. M., Reeves J. N., 2007, *MNRAS*, 382, 194
- Netzer H. 1990, in *Active Galactic Nuclei*, ed. R. D. Blandford, H. Netzer, L. Woltjer (Berlin: Springer), 137
- Reynolds C. S., 2019, *Nat. Astron.*, 3, 41
- Reynolds C. S., 2021, *ARA&A*, 59, 117
- Risaliti G., 2002, *A&A*, 386, 379
- Rivers E., Markowitz A., Rothschild R., 2011, *ApJS*, 193, 3
- Ross R. R., Fabian A. C., 2005, 358, 211
- Saha T., Markowitz A. G., Buchner J., 2022, *MNRAS*, 509, 5485
- Shirai H. et al., 2008, *PASJ*, 60, S263
- Shu X. W., Yaqoob T., Wang J. X., 2011, *ApJ*, 738, 147
- Takahashi T. et al., 2007, *PASJ*, 59, 35
- Tanaka Y. et al. 1995, *Nat.*, 375, 659
- Tanimoto A., Ueda Y., Odaka H., Kawaguchi T., Fukazawa Y., Kawamuro T., 2019, *ApJ*, 877, 95
- Thorne K. S., 1974, *ApJ*, 191, 507
- Tombesi F. et al. 2015, *Nat.*, 519, 436
- Turner T. J., George I. M., Nandra K., Mushotzky R. F. 1997, *ApJ*, 488, 164

- Tzanavaris P., Yaqoob T., LaMassa S., Ptak A., Yukita M., 2021, *ApJ*, 922, 85
 Ursini F., Bassani L., Malizia A., Bazzano A., Bird A. J., Stephen J. B., Ubertini B., 2019, *A&A*, 629, A54
 Walton D. J., Nardini E., Fabian A. C., 2013, *MNRAS*, 428, 2901
 Woo J.-H., Urry C. M., 2002, *ApJ*, 581, L5
 Wong K. C. et al., 2020, *MNRAS*, 498, 1420
 Yaqoob T., 2012, *MNRAS*, 423, 3360
 Yaqoob T., Edelson R., Weaver K. A., Warwick R. S., Mushotzky R. F., Serlemitsos P. J., Holt S. S., 1995, *ApJ*, 453, L81
 Yaqoob T., Murphy K. D., 2010, *MNRAS*, 412, 277
 Yaqoob T., Murphy K. D., 2011, *MNRAS*, 412, 1765
 Yaqoob T., Tatum M. M., Scholtes A., Gottlieb A., Turner, T. J., 2015, *MNRAS*, 454, 973
 Yi H., Wang J., Shu X., Fabbiano G., Pappalardo C., Wang C., Yu H., 2021, *ApJ*, 908, 156

APPENDIX A: COMPARISON WITH PREVIOUS X-RAY SPECTRAL STUDIES OF NGC 4388

In this section we summarize results from previous studies of NGC 4388, from observations with *Suzaku* and other X-ray astronomy missions. Since there are a large number of observations, rather than sequentially describe results from every mission, we give the principal results organized by particular spectral features or characteristics. We focus only on those results that are relevant for placing our results for the *Suzaku* spectral data into context. In particular, we do not go into great detail about the soft X-ray spectrum (below ~ 2 keV), because the present paper is concerned with the Fe $K\alpha$ line and Compton-reflection continua. Some comparisons of our results with historical ones are given in the main body of the present paper and are not necessarily repeated here.

Table A1 shows the principal X-ray missions that have observed NGC 4388 since *ASCA*, and the associated principal references for studies that have been published using the data. Note that the extended Fe $K\alpha$ emission in the *Chandra* data reported by Yi et al. (2021) has less than 2 per cent of the flux of the Fe $K\alpha$ line from the nuclear region. This means that in data that are not spatially resolved (i.e., all other data represented in Table A1), the extended component makes a negligible contribution to the observed Fe $K\alpha$ line. Note that the Shu et al. (2011) study is based in *Chandra* grating data, so also does not spatially resolve the Fe $K\alpha$ line. Also note that some of the studies that are cited use data from more than one mission, so some of the references in Table A1 are repeated.

After Shirai et al. (2008), results for the same *Suzaku* data were also published by Miyazawa et al. (2009), Lubiński et al. (2016), Fukazawa et al. (2011, 2016), and Kawamuro et al. (2019). The study by Fukazawa et al. (2016) was entirely focussed on the Fe $K\alpha$ and Ni $K\alpha$ emission-line features, and the analysis was restricted to the 5–9 keV energy band. The work by Lubiński et al. (2016) combined non-simultaneous INTEGRAL, *XMM-Newton*, and *Suzaku* spectra, so the model fits are compromised because of well-known spectral and flux variability. Also, although they included a Gaussian component for the narrow Fe $K\alpha$ line, they did not give any spectral-fitting results for the line. Therefore, the Lubiński et al. (2016) results will not be mentioned further.

Flux and Luminosity

The continuum flux from NGC 4388 varies by an order of magnitude across historical observations, the 2–10 keV flux ranging from $\sim 0.6 \times 10^{-11}$ erg cm $^{-2}$ s $^{-1}$ to $\sim 6 \times 10^{-11}$ erg cm $^{-2}$ s $^{-1}$. The 2–10 keV flux during the *Suzaku* observation is $\sim 2 \times 10^{-11}$ erg cm $^{-2}$ s $^{-1}$ (Table 3), so it is in the upper end of the historical range. The 2–10 keV observed luminosity during the *Suzaku* observation is $\sim 3 \times 10^{42}$ erg s $^{-1}$. The intrinsic luminosity is model-dependent, and we reported the values we obtained from modelling the *Suzaku* spectrum in Table 3, which shows 2–10 keV values in the range $\sim 7.4\text{--}8.1 \times 10^{42}$ erg s $^{-1}$. Thus, historical observations suggest that the intrinsic luminosity could be greater than 2×10^{43} erg s $^{-1}$ at times.

Column Density

The column density in NGC 4388 is known to be variable, and the historical range is $N_{\text{H}} \sim 2$ to 7×10^{23} cm $^{-2}$. However, except for analyses of the *NuSTAR* data (Kamraj et al. 2017; Masini et al. 2019) and the *NICER* data (Miller et al. 2019), all of the other column density measurements are obtained from simple one-dimensional models of the extinction. Shirai et al. (2008) reported column densities in the range ~ 2.3 to 4.1×10^{23} cm $^{-2}$ from various phenomenological fits to the *Suzaku* spectrum. Miyazawa et al. (2009) and Fukazawa et al. (2011) obtained values consistent with that range for the same *Suzaku* data. We obtained a column density of $\sim 2.6 \times 10^{23}$ cm $^{-2}$ for a uniform spherical model for the same data. For MYTORUS model fits we obtained $\sim 3 \times 10^{23}$ cm $^{-2}$ for the line-of-sight absorption (see Table 2). The decoupled version of the MYTORUS model gave a global column density of $\sim 6 \times 10^{23}$ cm $^{-2}$. By comparison, coupled MYTORUS fits to the *NuSTAR* data gave a column density of $\sim 6.5 \times 10^{23}$ cm $^{-2}$ (Kamraj et al. 2017), and decoupled MYTORUS fits to the *NuSTAR* data gave a column density of $\sim 4.4 \times 10^{23}$ cm $^{-2}$ (Masini et al. 2019). The *NICER* data gave a column density of $\sim 2.6 \times 10^{23}$ cm $^{-2}$ (Miller et al. 2019) for the coupled MYTORUS model. All of these measurements are consistent with a clumpy distribution of matter, which has an average global column density of $\sim 7 \times 10^{23}$ cm $^{-2}$, with clumps moving in and out of the line of sight, resulting in a variable line-of-sight column density.

Narrow Fe $K\alpha$ Emission Line

The best measurement of the (rest-frame) centroid energy of the narrow Fe $K\alpha$ line is still that from a *Chandra* HETG observation (Shu et al. 2011), its value of 6.393 ± 0.004 keV being consistent with the weighted mean of the $K\alpha_1$ and $K\alpha_2$ components from neutral Fe (subject to calibration systematics and velocity shifts relative to the galaxy redshift). All other historical observations are consistent with this, but the different instruments have larger systematic and statistical errors than the *Chandra* HETG data. In our modelling of the narrow Fe $K\alpha$ line, the energies of the $K\alpha_1$ and $K\alpha_2$ components are fixed by physics, but we allowed a shift to account for possible calibration systematics and/or velocity shifts. We also concluded that the data are consistent with neutral Fe, with a systematic, expressed as a net velocity blueshift, of $700\text{--}900$ km s $^{-1}$, depending on the model.

For the narrow Fe $K\alpha$ line, we obtained a line flux of $\sim 9.0 \times 10^{-5}$ photons cm $^{-2}$ s $^{-1}$ from the spherical model, and $\sim 8.7 \times 10^{-5}$ photons cm $^{-2}$ s $^{-1}$ from both implementations of the MYTORUS model. We obtained an equivalent width of 257 eV from the spherical model, and 255 eV from both implementations of the MYTORUS model. All except the *Swift* study by Ferodova et al. (2011) gave explicit Fe $K\alpha$ line fluxes. The Fe $K\alpha$ line flux reported for observations by other missions, clusters in the range $\sim 7\text{--}9 \times 10^{-5}$ photons cm $^{-2}$ s $^{-1}$, but on one occasion, in a 2011 *XMM-Newton* observation, a lower value of $5.7 \pm 0.8 \times 10^{-5}$ photons cm $^{-2}$ s $^{-1}$ was reported (Ursini et al. 2019). Except for this latter observation, for the studies that do report an explicit line flux, the

Table A1. Historical X-ray Spectral Studies of NGC 4388

Mission	References
<i>ASCA</i>	Iwasawa et al. 2007
<i>BeppoSAX</i>	Risaliti et al. 2002
<i>RXTE</i>	Elvis et al. 2004
	Rivers et al. 2013
<i>INTEGRAL</i>	Beckmann et al. 2004
	Fedorova et al. 2011
	Ursini et al. 2019
	Lubiński et al. 2016
<i>Chandra</i>	Shu et al. 2011
	Yi et al. 2021
<i>XMM-Newton</i>	Elvis et al. 2004
	Beckmann et al. 2004
	Ursini et al. 2019
	Lubiński et al. 2016
<i>Suzaku</i>	Shirai et al. 2008
	Miyazawa et al. 2009
	Fukazawa et al. 2011
	Kawamuro et al. 2019
	Lubiński et al. 2016
<i>Swift</i>	Fedorova et al. 2011
	Kawamuro et al. 2019
<i>NuSTAR</i>	Masini et al. 2016
	Kamraj et al. 2017
	Ursini et al. 2019
<i>NICER</i>	Miller et al. 2019

values are within $\sim 20\%$, or less, of our measurements from the *Suzaku* spectrum. Note that fluxes across different missions are not adjusted for absolute flux calibration systematics, which can be more than 10 per cent in some cases.

The Fe $K\alpha$ line equivalent width reported in studies based on observations with different X-ray astronomy missions has a wide range, from ~ 50 eV, to ~ 700 eV. These results are consistent with a picture in which the Fe $K\alpha$ line flux remains steady most of the time, not responding to continuum variations, whilst the equivalent width varies as the continuum varies. We note that the lowest values of the equivalent width are 50 ± 10 eV and 73 ± 5 eV, from a 2011 *XMM-Newton* observation (Ursini et al. 2019), and the *NICER* observation (Kamraj et al. 2017) respectively. The continuum luminosity during these observations was at the upper end of the historical range, and during the time of the *NICER* observation, the continuum was a factor ~ 3 higher than it was during the *Suzaku* observation.

As for the narrow Fe $K\alpha$ line width, the best measurement of its width is that from a *Chandra* HETG observation (Shu et al. 2011), because the HETG data have the highest spectral resolution, which is ~ 1860 km s $^{-1}$ FWHM, at 6.4 keV, which is a factor of ~ 3 higher than CCD resolution. The HETG line width is 2430_{-590}^{+620} km s $^{-1}$ FWHM, which compares well with our measurements from the *Suzaku* spectrum (the highest value in Table 2 is 3415_{-590}^{+740} km s $^{-1}$ FWHM), despite the poorer spectral resolution. Shirai et al. (2008) gave a Gaussian line width of 45_{-6}^{+5} eV for the same *Suzaku* data, which corresponds to a FWHM of 4965 km s $^{-1}$. Their statistical errors appear to be too small, and their larger width is due to the fact that they used phenomenological models, whereas our widths are based on physical models, and are closer to the *Chandra* HETG measurement, which is less model-dependent than CCD measurements. Miller et al. (2019) gave a Gaussian line width of 40 ± 10 eV from the *NICER* data, which corresponds to 4433 km s $^{-1}$ FWHM (but note that the FWHM given by Miller et al. (2019) is incorrect, because it does not correspond to their Gaussian width). Measurements of the Fe $K\alpha$ line width from *XMM-Newton* data (Elvis et al. 2004, Beckmann et al. 2004) gave even larger values than Shirai et al. (2008), in the region of ~ 7300 – 8500 km s $^{-1}$ FWHM. All of these large widths from CCD measurements are again due to the use of phenomenological models. Ursini et al. (2019) do not give any line width constraints from their *XMM-Newton* analysis, nor do Fedorova et al. (2011) from their *Swift* analysis. All other studies shown in Table A1 are based on non-CCD instruments, and have much worse spectral resolution than CCDs, so Fe $K\alpha$ line width measurements from those data are not informative.

Shirai et al. (2008) and Kawamuro et al. (2016) included an additional Gaussian Compton shoulder component for the Fe $K\alpha$ line, and forced its flux to be a fixed percentage of the core (unscattered) Fe $K\alpha$ line. However, this empirical model has the wrong shape for the Compton shoulder, and its strength relative to the unscattered line component should depend on the column density and geometry of the line-emitting matter. Moreover, Yaqoob and Murphy (2010) showed that it is not possible, even in principle, to detect the Compton shoulder with CCD detectors. In contrast, all of the models that we applied to the *Suzaku* data in the present paper self-consistently include the Compton shoulder, so it is not an *ad hoc* component in our models. In any case, the Compton shoulder makes an insignificant contribution to the Fe $K\alpha$ line profile for the column densities involved, which is why it cannot be seen in the data or models (e.g., see Yaqoob and Murphy 2010).

Reflection Continuum and Broad Fe $K\alpha$ Emission Line

Historical X-ray spectral studies of NGC 4388 (Table A1) have either included no Compton-reflection continuum (ASCA, Iwasawa et al. 1997), or they have fitted the nonrelativistic, neutral disk-reflection model PEXRAV (Magdziarz and Zdziarski, 1995), or PEXMON (Nandra et al. 2007). The latter includes an associated (narrow) Fe $K\alpha$ emission line, whereas PEXRAV does not. Only the *NICER* study (Miller et al. 2019) used PEXMON, the rest used PEXRAV. Some of the studies state that the Compton-reflection component is included to model actual X-ray reflection from a disk, whereas other studies state that they are using PEXRAV to model Compton-reflection from the obscuring material that is also responsible for the X-ray absorption. In the former case, Compton-reflection

from the obscuring material should have been included (because there has to be some associated with the neutral obscuring material that produces the Fe K α line). In the latter case, the use of PEXRAV as a surrogate is problematic. The reason is that the shape of a Compton-reflection continuum depends on the column density and the geometry, amongst other things (e.g. Murphy & Yaqoob 2009; Brightman and Nandra 2011), and the Fe K α emission line has to be added in as an *ad hoc* empirical component, whereas it is physically tied to the geometry and column density of the same material producing the Compton-reflection continuum.

The fact that PEXRAV is not appropriate for modelling the Compton-reflection continuum from the distribution of obscuring matter has resulted in different studies making different assumptions about the value at which the disk inclination angle in the PEXRAV model should be fixed. This inclination angle is meaningless when a disk geometry is used as a surrogate for a geometry that is not a disk, and different authors have fixed it at one of several values between 30° and 78°. Shirai et al. (2008) even admit that the choice of the inclination angle affects the conclusion about the value of the so-called ‘reflection fraction’ parameter, R , which is 1.0 for a disk that subtends a solid angle of 2π at the X-ray source, which is non-variable and illuminates the disk from a point on its axis. The inclination angle cannot be left as a free parameter, because it would lead to the awkward problem of interpreting a meaningless parameter in the context that the model is used. X-ray reprocessor spectral-fitting models that self-consistently account for absorption, and its associated Compton-reflection and Fe K α fluorescence emission-line, were readily available for work published in 2011 or later, but only the *NuSTAR* (Masini et al. 2016; Kamraj et al. 2017) and *NICER* (Miller et al. 2019) studies made use of such models (specifically, they applied the MYTORUS model). These studies did also compare the results from fitting the MYTORUS model with the results of fitting PEXRAV (*NuSTAR*) or PEXMON (*NICER*).

Notwithstanding the caveats outlined above, the over-arching conclusion from the historical works that included the PEXRAV or PEXMON models, is that all except Shirai et al. (2008), concluded that these components are not strongly required by the data, and only upper limits on the R parameter were obtained. The upper limits on R range from 0.09 (*NuSTAR*, Kamraj et al. 2017) to 0.8 (one of the joint *XMM-Newton/RXTE* observations, Elvis 2004). Note that a small, non-zero value of $R = 0.113^{+0.006}_{-0.007}$ was reported by Miller for the *NICER* data, but those data do not extend beyond ~ 10 keV, so the very small errors on R are incongruent with the limited capability of the data to constrain any Compton-reflection continuum (which, for PEXRAV and PEXMON peaks around ~ 20 – 30 keV). Moreover, Miller et al. (2019) state that the PEXMON inclination angle was fixed at 5°, but the model does not allow inclination angles below 18.2°.

Shirai et al. (2008) fitted various combinations of models to the *Suzaku* X-ray spectrum, and obtained various values of R that were model-dependent, but all greater than unity, with non-zero lower limits. This discrepancy compared to all the other studies is likely to be due to several reasons. One is that, as Shirai et al. (2008) point out, the background-subtraction for the high-energy *Suzaku* data was not yet sufficiently accurate at that time. Another is that Shirai et al. (2008) allowed the relative normalization between the CCD instrument (XIS) and high-energy instrument (HXD) to be a free parameter, since cross-instrument calibration had not yet matured. They also fixed the inclination angle of the PEXRAV model at 78°, a value that is higher than in any other study. There is degeneracy in the inclination angle and R parameters, such that more edge-on values of the inclination angle require greater values of R to achieve the same magnitude of the reflection continuum relative to the direct continuum. A later work by Kawamuro et al. (2016) obtained $R = 0.08^{+0.05}_{-0.04}$ from the same *Suzaku* data. Note that Miyazawa et al. (2009) and Fukazawa et al. (2011) also analyzed the same *Suzaku* data, and included a PEXRAV model component, but they did not actually reveal any results for any of the fitted PEXRAV parameters.

Only one of the studies in Table A1 (Shirai et al. 2008) explicitly tested the NGC 4388 data for a relativistically-broadened Fe K α line, in the form of a discrete, *ad hoc* emission-line with a shape based on Doppler and gravitational energy shifts. They obtained only an upper limit on the equivalent width of 110 eV. However, given the *ad hoc* nature of the other model components, an interpretation of this result is not clear. Miller et al. (2019) did apply a relativistic blurring kernel model, RDBLUR (Fabian et al. 1989), to their PEXMON component, but the purpose of that was to attempt to constrain the inner extent of the narrow Fe K α line-emitting material. Note that Miller et al. (2019) state that the inclination angle in the RDBLUR model was fixed at 5°, but the model does not allow inclination angles below 18.2°. Only one of the studies (Kawamuro et al. 2016) fitted a full relativistic disk model that includes both the reprocessed continuum emission and broadened emission lines. The model that was fitted was that of the ionized disk model REFLIONX (Ross and Fabian 2005), convolved with RDBLUR. However, they found that for NGC 4388, the model did not improve the fit, resulting in a small upper limit on the effective R value, of 0.03.

Fe Abundance

If an Fe abundance is derived from phenomenological models consisting of *ad hoc* components that are not physically self-consistent, then that Fe abundance must be interpreted as just a parameter, and not an actual Fe abundance. Specifically, an Fe abundance obtained from fitting an *ad hoc* component for the Fe K α emission line, combined with a PEXRAV component to model the Compton reflection continuum from the material producing the line, is not self-consistent. Moreover, the inclination angle in the PEXRAV component is fixed at an arbitrary value, since the model has an inappropriate geometry. Shirai et al. (2008) fitted these model components to *Suzaku* data, leaving the Fe abundance in the PEXRAV model a free parameter. They obtained different values, all sub-solar, for different variations on the overall model. However, these values of the Fe abundance are not a measure of the abundance. In our fit to the same *Suzaku* data using the uniform spherical model, the Fe K α emission line, the extinction, and the Compton reflection are all physically self-consistent, so our value of $1.102^{+0.024}_{-0.021}$ for the Fe abundance relative to the assumed solar value, is the most robust measurement of the Fe abundance from the X-ray spectrum of NGC 4388 to date.

Ionized Wind

In our analysis of the *Suzaku* spectrum of NGC 4388 we found absorption lines due to He-like and H-like Fe, indicative of a highly ionized wind. Both of these features have been reported from a 2011 *XMM-Newton* observation (Ursini et al. 2019), and the He-like feature has been reported by Shirai et al. (2008) from the same *Suzaku* data, and by Miller et al. (2019) from the *NICER* data. Although the *Chandra* HETG has better spectral resolution than CCD data, neither absorption line has been reported for existing *Chandra* HETG data, most likely due to the limited statistics of these data.